The Astrophysical Journal, 961:217 (16pp), 2024 February 1 https://doi.org/10.3847/1538-4357/ad0e63

# A Dynamic Galaxy: Stellar Age Patterns across the Disk of M101

Ray Garner, III[1,2,4], J. Christopher Mihos[1], Paul Harding[1], and Charles R. Garner, Jr.[3]
[1] Department of Astronomy, Case Western Reserve University, 10900 Euclid Avenue, Cleveland, OH 44106, USA
[2] Department of Physics and Astronomy, Texas A&M University, 578 University Drive, College Station, TX 77843, USA
[3] Rockdale Magnet School for Science and Technology, 930 Rowland Road, Conyers, GA 30012, USA; ray.garner@tamu.edu

*Received 2023 September 15; revised 2023 November 10; accepted 2023 November 19; published 2024 January 29*

## Abstract

Using deep, narrowband imaging of the nearby spiral galaxy M101, we present stellar age information across the full extent of the disk of M101. Our narrowband filters measure age-sensitive absorption features such as the Balmer lines and the slope of the continuum between the Balmer break and 4000 Å break. We interpret these features in the context of inside-out galaxy formation theories and dynamical models of spiral structure. We confirm the galaxy's radial age gradient, with the mean stellar age decreasing with radius. In the relatively undisturbed main disk, we find that stellar ages get progressively older with distance across a spiral arm, consistent with the large-scale shock scenario in a quasi-steady spiral wave pattern. Unexpectedly, we find the same pattern across spiral arms in the outer disk as well, beyond the corotation radius of the main spiral pattern. We suggest that M101 has a dynamic, or transient, spiral pattern with multiple pattern speeds joined together via mode coupling to form coherent spiral structure. This scenario connects the radial age gradient inherent to inside-out galaxy formation with the across-arm age gradients predicted by dynamic spiral arm theories across the full radial extent of the galaxy.

*Unified Astronomy Thesaurus concepts:* Galaxy ages (576); Galaxy dynamics (591); Stellar ages (1581); Narrow band photometry (1088); Galaxy evolution (594)

## 1. Introduction

Spiral galaxies are believed to have formed "inside-out," that is the inner parts of galactic disks form first, followed by the formation of their outer regions (e.g., White & Frenk 1991; Mo et al. 1998). One notable consequence of inside-out formation is a radial variation in the star formation history (SFH), and thus stellar ages, of a spiral galaxy. These have been primarily observed as a color gradient in the disk, in that inner regions appear redder (older) than the bluer (younger) outer regions (e.g., de Jong 1996; Bell & de Jong 2000; MacArthur et al. 2004). Complicating this picture are nonaxisymmetric structures in the disk, such as spiral arms, that both radially scatter stars (e.g., Sellwood & Binney 2002; Roškar et al. 2008a, 2008b) and imprint azimuthal variations in the stellar age distribution (e.g., Dixon 1971; Dobbs & Pringle 2010; Chandar et al. 2017).

Understanding the nature and creation mechanism of spiral structure in galaxies is still a fundamental problem in astronomy. We lack a complete and widely accepted theory for the origin of spiral patterns. Many spiral galaxies have structure driven by nonaxisymmetric effects, whether that be caused by external interactions with a companion (Kormendy & Norman 1979; D'Onghia et al. 2016; Pettitt et al. 2016) or by internal responses to a centrally rotating bar (Contopoulos & Papayannopoulos 1980; Athanassoula 1992). There is also the possibility that some spiral structure is self-excited. Broadly speaking, there are two possible mechanisms for self-excitation. First, there is the "density wave theory" that argues that spiral structure is the result of a quasi-steady global mode in the stellar disk (Lin & Shu 1964; Bertin et al. 1989). Second, there is the suggestion that spiral structure is caused by transient and recurrent instabilities resulting in "dynamic" spiral arms that appear and reappear in cycles (Toomre 1964; Sellwood & Carlberg 1984; Elmegreen & Elmegreen 1986; Sellwood & Kahn 1991). We will refer the interested reader to any number of reviews on spiral mechanisms for more detailed information (e.g., Dobbs & Baba 2014; Shu 2016; Sellwood & Masters 2022).

Clearly there are multiple spiral pattern generation mechanisms, and we must turn to observations and simulations of spiral galaxies to inform us which is the primary mechanism. However, as highlighted by Sellwood (2011), it is very difficult to find observational tests to distinguish between these theoretical models. As an example, in the standard density wave theory, spiral arms are density waves moving with a constant pattern speed. Inside corotation (the radius at which the angular speed of stars and gas equals the pattern speed), material will rotate faster than the spiral pattern. When gas enters the spiral pattern, it may experience a shock and collapse to form stars (Roberts 1969; Shu et al. 1972; see McKee & Ostriker 2007 and references therein for an extensive discussion of the theory). As these stars age, they overtake the more slowly rotating spiral pattern, drifting away from their birth sites and creating an azimuthal age gradient across the spiral arm (Figure 1; see also Figure 1 in Martínez-García et al. 2009). We would then expect to find young star clusters near the spiral arm along the leading edge and older stars further along, approaching the trailing side of the next spiral arm. Outside of corotation, the spiral pattern moves faster than the gas, and the opposite sequence occurs (Dixon 1971).

Numerous simulations have been performed in recent years to test this theory. For example, Dobbs & Pringle (2010) found that in galaxies with a constant pattern speed, a clear age

---

[4] Corresponding author.

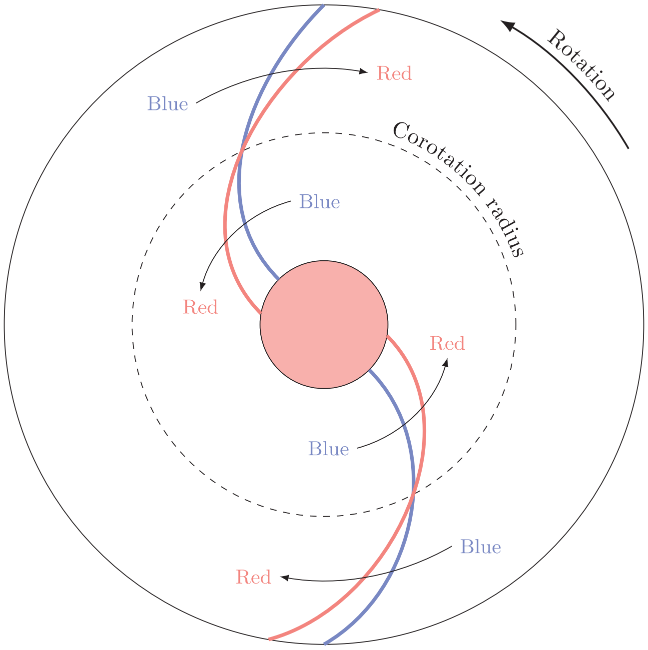

**Figure 1.** Schematic of the shock scenario posited by Roberts (1969). Stellar age gradients across the spiral arms are indicated by arrows that go from blue to red. The azimuthal age gradients are produced by stars born in the spiral shock, where the shocked interstellar medium (ISM) forms a dust lane, and later drift away as they age. The direction of the gradients flips at the corotation radius. Inside corotation, the gas and stars overtake the spiral pattern, and outside corotation, the spiral pattern overtakes the gas and stars.

sequence across spiral arms from young to old stars is expected. This pattern was absent in dynamic and tidally disturbed galaxies. Subsequent simulations with more advanced hydrodynamical modeling have confirmed the case for the latter pair of spiral arm mechanisms (Wada et al. 2011; Grand et al. 2012; D'Onghia et al. 2013; Baba et al. 2015, 2017; Dobbs et al. 2017; Pettitt et al. 2017). Observationally, evidence of the large-scale shock scenario is hard to come by except in a few cases. Martínez-García et al. (2009) studied color gradients across the spiral arms of 13 spiral galaxies, 10 of which had the expected color gradient. They have since found color gradients for a few more galaxies (Martínez-García & González-Lópezlira 2011, 2015). Similarly, Sánchez-Gil et al. (2011) produced age maps of six nearby galaxies using the H$\alpha$/FUV flux ratio, only two of which (M74 and M100) presented an age gradient across spiral arms. Investigating resolved stellar clusters in three galaxies, Abdeen et al. (2022) found evidence of the expected age gradients in galaxies where others have not. Simply put, with the exception of a handful of specific cases, there is no clear systematic trend in the observations.

Some of the observational ambiguity likely comes from the wide use of broadband colors to discern age gradients. The well-known age–metallicity degeneracy (Worthey 1994), combined with the reddening effects of dust, blurs the conclusions made with color gradients. Spectroscopy gives the ability to break this degeneracy by resolving multiple age- and metallicity-sensitive absorption features. However, spectroscopy becomes prohibitively expensive to measure the low surface brightness (LSB) outskirts of disk galaxies. For nearby galaxies with large angular sizes—where we can resolve physically small scales—most integral field units are also not large enough to cover the whole galaxy without resource-intensive mosaicking techniques.

Another alternative to broadband photometry is narrowband photometry, particularly observations targeting age-diagnostic absorption features like the Balmer lines, the 4000 Å break, or metallic lines such as Mg b. Pioneering narrowband work has been performed for spiral galaxies (Beauchamp & Hardy 1997; Mollá et al. 1999; Ryder et al. 2005), and modern narrowband photometry can measure absorption line strengths that are compatible with spectroscopy (Stothert et al. 2018; Angthopo et al. 2020; Renard et al. 2022). Absorption line equivalent widths (EWs) are largely insensitive to dust effects (MacArthur 2005) and, combined with stellar population synthesis modeling, have been used to investigate luminosity-weighted stellar ages in integrated stellar populations (e.g., Fisher et al. 1995; Ganda et al. 2007; Sánchez-Blázquez et al. 2014a, 2014b).

In an effort to study stellar ages and their connection to the nature of spiral patterns, we have used Case Western Reserve University's (CWRU's) Burrell Schmidt 24/36 inch telescope and its accompanying narrowband filters to image the nearby spiral galaxy M101 (NGC 5457). While these images targeting H$\alpha$, H$\beta$, [O III] $\lambda\lambda$4959,5007, and [O II] $\lambda\lambda$3726,3729 have been used to study the emission line properties of M101 and its group environment (Watkins et al. 2017; Garner et al. 2021, 2022), these images also reveal age-diagnostic absorption signatures in the stellar disk of M101 (Figure 2). Thus, by measuring EWs through our narrowband filters, we are able to place constraints on the stellar ages throughout M101's disk.

M101 was chosen for this survey because its nearby distance ($D = 6.9$ Mpc; see Matheson et al. 2012 and references therein) enables its properties to be studied in great detail at high spatial resolution. Indeed, Lin et al. (2013) performed a pixel-based multiwavelength spectral energy distribution (SED) fitting and broadly found that M101 supports the inside-out disk growth scenario with detections of radial stellar age and metallicity gradients. The disk of M101 also has a dynamic nature: it has strong morphological asymmetries (e.g., Beale & Davies 1969), complex H I kinematics (e.g., Waller et al. 1997; Mihos et al. 2012; Xu et al. 2021), a Type I extended-UV disk (Thilker et al. 2007), and faint tidal features to the northeast and east (Mihos et al. 2013, 2018). These are all likely signatures of an interaction M101 had with its most massive satellite, NGC 5474, about 300 Myr ago (Linden & Mihos 2022). Thus, M101 provides an interesting, albeit often overlooked, testing ground for the varying roles of self-excited and tidally induced spiral patterns.

## 2. Narrowband Observations

The narrowband imaging data for this project were taken over four observing seasons using CWRU Astronomy's 24/36 inch Burrell Schmidt telescope located at Kitt Peak Observatory. Full details of our narrowband imaging techniques are given in Watkins et al. (2017) and Garner et al. (2022). Quantitative information about the narrowband filters and final imaging stacks for the data set is given in Table 2 of Garner et al. (2022). Briefly, we summarize our observations here.

Our data set consists of a set of narrow on-band filters ($\Delta\lambda \approx 80$–$100$ Å) centered on the redshifted emission lines H$\alpha\lambda$6563, H$\beta\lambda$4861, [O III] $\lambda\lambda$4959,5007, and [O II] $\lambda\lambda$3727,3729. To measure the adjacent stellar continuum for each line, we also observed M101 in narrow off-band filters

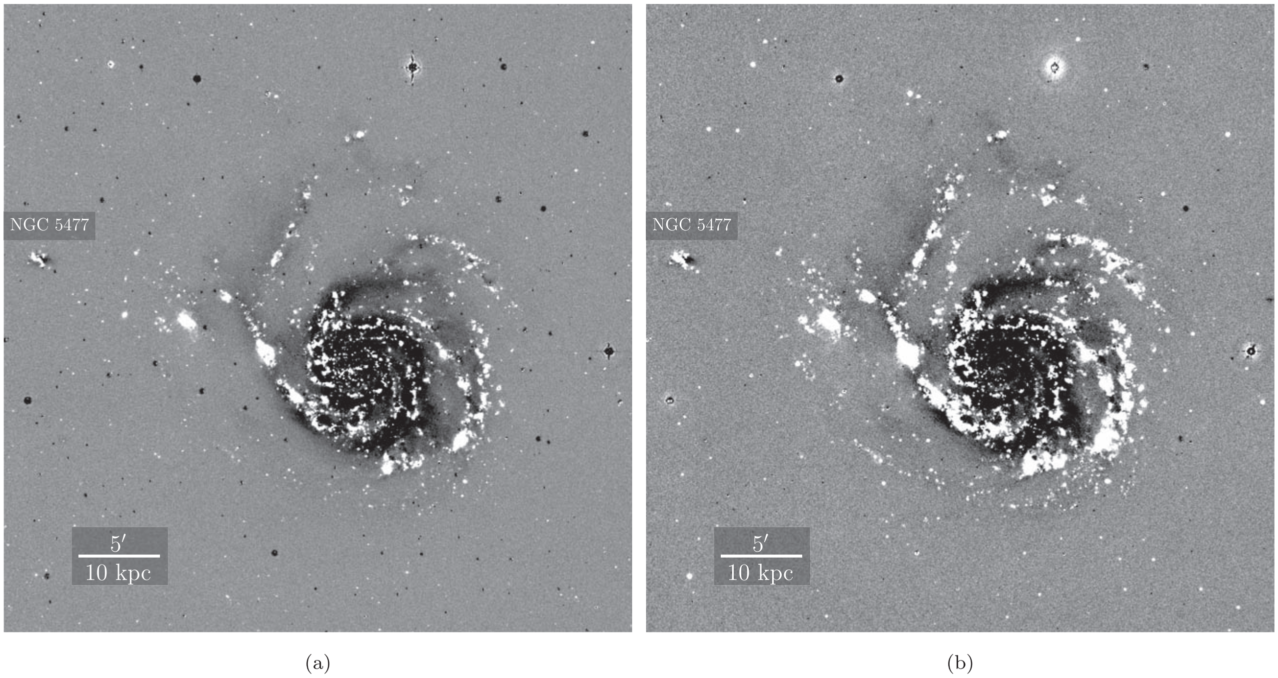

(a) (b)

**Figure 2.** (a) The continuum-subtracted H$\beta$ image. (b) The continuum-subtracted [O II] image. Images are scaled in such a way that emission line objects are in white and absorption features are in black. Note the strong absorption features in the disk of M101. The satellite galaxy NGC 5477 is marked to the left, and a scale bar is provided. The image measures $40' \times 40'$. North is up, and east is to the left.

shifted in wavelength by ≈100–150 Å from each on-band filter. The Burrell Schmidt images a $1\overset{\circ}{.}65 \times 1\overset{\circ}{.}65$ field of view onto a $4096 \times 4096$ back-illuminated CCD, yielding a pixel scale of $1\farcs45$ pixel$^{-1}$. In each filter, we took 50–70 1200 s images of the galaxy, randomly dithering the telescope by $10'$–$30'$ between exposures. Both twilight flats and night sky flats were taken throughout each observing run, as were images of spectrophotometric standards and bright stars to assist with photometric calibration and scattered-light modeling, respectively.

All observed images are treated to the data reduction procedures described by Watkins et al. (2017) and Garner et al. (2022). Namely, the steps are as follows: (1) subtraction of the bias frame, (2) flat-field correction, (3) removal of scattered light from bright stars following the technique of Slater et al. (2009), (4) registration of the stacked images, and (5) flux calibration of the stacked images. We flux calibrated the final image stacks using a variety of techniques: (1) deriving a photometric solution from observations of Massey et al. (1988) spectrophotometric standard stars, (2) measuring zero-points from *ugr* magnitudes of the ∼150 stars in the M101 field from the Sloan Digital Sky Survey (SDSS), and, (3) where possible, synthesizing narrowband magnitudes using SDSS spectroscopy of ∼100 point sources in the M101 field. These different techniques yielded flux zero-points that agreed to within ±5%, which we take to be the absolute flux uncertainties in the data.

Previously, we used these narrowband images of M101 and its group environment to investigate emission line sources, whether in the intragroup environment (Garner et al. 2021) or within the disk of M101 and its satellites (Watkins et al. 2017; Garner et al. 2022). However, the level of precision and accuracy of our imaging and reduction techniques reveals absorption signatures in the images, particularly in the H$\beta$ and [O II] continuum-subtracted images. We focus on these two images out of our narrowband data set, since our [O III] filters do not sample any strong stellar absorption features, and while trends in H$\alpha$ absorption are similar to the H$\beta$ absorption, H$\alpha$ absorption is less sensitive to age than H$\beta$ (e.g., González Delgado et al. 2005). Figure 2 shows the H$\beta$ and [O II] continuum-subtracted images, and within the disk of M101, darker regions are present. We stress that this is not incorrect off-band oversubtraction in our data reduction techniques but rather the presence of absorption signatures caused by the underlying older stellar population.

In order to focus only on features in the stellar continuum, we need to mask both foreground stars and strong emission line H II regions in M101. We follow the techniques described by Garner et al. (2022) to remove foreground Milky Way stars from our images. We masked those stars in the Tycho-2 Catalog (Høg et al. 2000) brighter than $B_T = 12.5$. All of these stars lie projected outside of the disk of M101. For fainter stars, we used the Two Micron All Sky Survey All-Sky Catalog of Point Sources (Skrutskie et al. 2006). We aggressively mask these stars using $8\farcs7$ apertures (roughly three times the FWHM of the point-spread function of the coadded image stacks). To mask H II regions, we used the segmentation map produced by Garner et al. (2022), which used `astropy`'s `PhotUtil` package and its `segmentation` module (Bradley et al. 2023) to identify bright H II regions using the continuum-subtracted H$\alpha$ image. Finally, we also mask the nearby satellite galaxy NGC 5477, visible in our images projected $22'$, or 44 kpc, to the east.

We note that although we have masked the brightest portions of the strongly emitting H II regions, there is still scattered emission and diffuse ionized gas (DIG) in our images. Briefly, scattered emission refers to light from bright H II regions scattered toward the observer by interstellar dust particles in M101's disk regardless of the ionization state of the gas (e.g.,

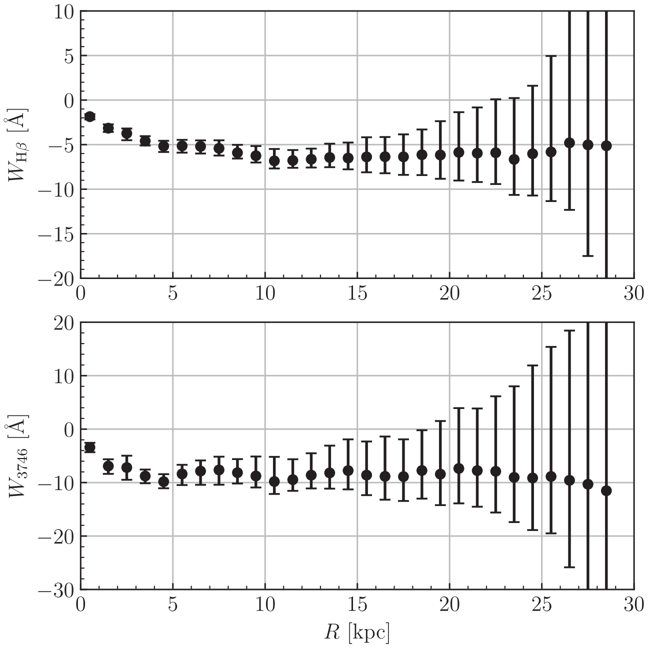

**Figure 3.** The radial profiles of the median stellar EWs measured through our H$\beta$ and [O II] filters, $W_{\mathrm{H}\beta}$ and $W_{3746}$, respectively. Radial bins have widths of 1 kpc (30″). The error bars indicate the quartile scatter of the EWs measured in each radial bin.

Brandt & Draine 2012 and references therein), while the DIG refers to the warm, low-density, ionized component of the interstellar medium (ISM; see Haffner et al. 2009 and references therein). The DIG has a varying presence throughout a galaxy, and so we correct for the DIG using the approach of Vale Asari et al. (2019). They separate the DIG from normal star-forming regions on the basis of the measured H$\alpha$ EW. Thus, the required correction as prescribed by Equation (2) of Vale Asari et al. (2019) is ∼5% in all of our narrowband observations, which we apply to our data. There is no similar correction for scattered light, but this will be strongest near H II regions, which we have aggressively masked.

As an example of the extent and depth of our data, Figure 3 shows the binned radial profiles of the median stellar EW (after masking H II regions) measured through our H$\beta$ and [O II] filters, $W_{\mathrm{H}\beta}$ and $W_{3746}$, respectively, out to 30 kpc (15′).[5] Importantly, the error bars are dominated by physical scatter in data rather than measurement error. The H$\beta$ EW, $W_{\mathrm{H}\beta}$, shows a negative gradient out to $R \sim 10$ kpc, beyond which it flattens, and the [O II] EW, $W_{3746}$, shows a negative gradient out to $R \sim 5$ kpc, similarly flattening beyond this radius. Interpretation of these trends is simplest for $W_{\mathrm{H}\beta}$, with the presence of A-type stars increasing with radius, subsequently deepening the H$\beta$ absorption line, although the scatter at large radius might suggest the presence of younger populations. However, the interpretation of the EW measured through the [O II] filters is less straightforward and motivates more detailed spectral modeling. Additionally, the large variance in EWs in the outer disk motivates treating the main and outer disks separately, where in the main disk we can explore any trends with respect to morphological environments.

## 3. Defining Environments within M101's Disk

Our goal is to construct morphological, environmental masks to allow us to study the stellar ages of different regions in M101's disk. In order to outline stellar structures, we utilize the broadband $B$ image of M101 (Mihos et al. 2013). In the following, we define several basic environments that are included in the masks: inner disk, spiral arms and interarm regions, and the main and outer disks.

### 3.1. The Inner Disk

In traditional photometric decompositions of galaxies, the exponential disk is usually distinguished from a central bulge component. Additionally, some galaxies have unresolved or marginally resolved stellar structures that are centrally concentrated. Some of these structures might be an unresolved nuclear bar, a nuclear ring, or a nuclear disk. Finally, at small radii, spiral arms and their interarm regions become increasingly hard to define in an objective manner.

In the specific case of M101, its morphological classification is that of a spiral galaxy without a large classical bulge (S$\underline{\mathrm{A}}$B (rs)c; Buta et al. 2015). It is known to have a mildly star-forming pseudobulge (Fisher et al. 2009; Fisher & Drory 2010; Kormendy et al. 2010) with an effective radius of 372 ± 436pc (11$''\!.$1 ± 13$''\!.$0; Fisher & Drory 2010). While other studies have resolved and studied the stellar age of the pseudobulge and surrounding region (Lin et al. 2013), since our focus is on the spiral arms and interarm regions, we visually define an inner disk region of 120″ (4 kpc). This encompasses the pseudobulge and the region where the spiral arms become so tightly wrapped they are hard to define. We note that this is much larger than what studies of morphological features have considered to be the central region, often <20″ (Lin et al. 2013; Querejeta et al. 2021).

### 3.2. Spiral Arms and Interarm Regions

In general, logarithmic spirals are good approximations to the shape of galactic spiral arms (Seigar & James 1998). Ubiquitous throughout nature, logarithmic spirals are easy to mathematically define (see Section 2 of Davis et al. 2017), but defining in a robust sense where the spiral arms are in a galaxy is more difficult. Over the years, numerous methods have been presented in the literature to define spiral arms and estimate their pitch angles (see Hewitt & Treuthardt 2020 and references therein). These methods, while useful for large surveys due to their (semi)automation, each come with their own issues. For instance, some methods may not always trace real three- or four-armed spiral patterns in galaxies, nor do they handle asymmetric arms well (Elmegreen et al. 1992). These methods also generally only model one global pitch angle for a galaxy, rather than accurately define a more complicated spiral pattern.

Since our focus is on M101 and its strongly asymmetric spiral pattern, we forgo these automated methods and instead adopt a different approach based on the visual inspection of the spiral arms. This allows for multiple pitch angles at different radii in M101 and takes into account that those pitch angles will be asymmetrical with respect to the galaxy center. Thus, we follow a semiautomatic procedure developed by the S$^4$G (Sheth et al. 2010) and PHANGS (Lee et al. 2022) teams in Herrera-Endoqui et al. (2015) and Querejeta et al. (2021), respectively. We briefly summarize those procedures and our slight modifications here.

---

[5] We note that $W_{3746}$ is named for the central wavelength of the on-band filter, not for the EW of any individual absorption line.

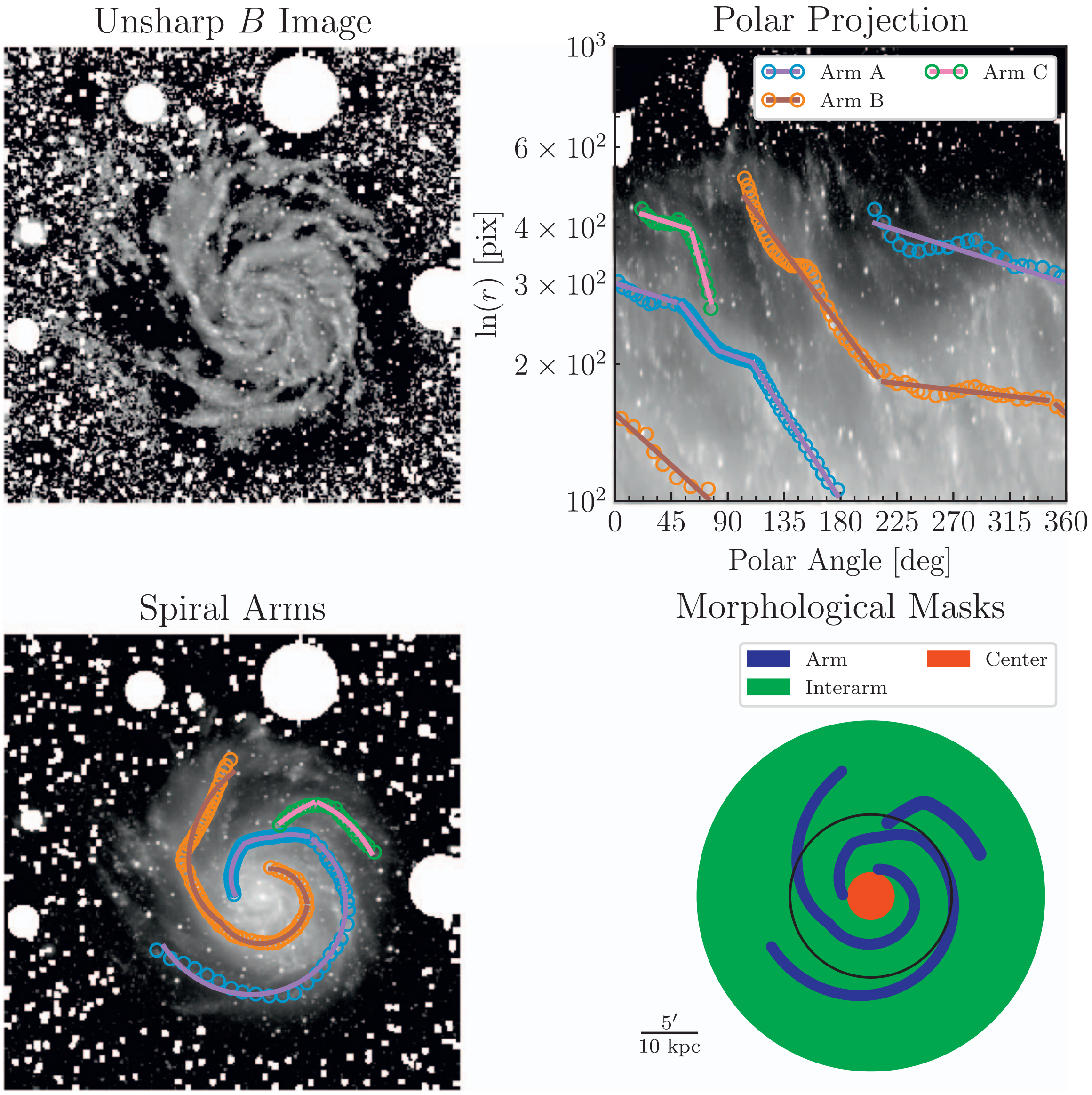

**Figure 4.** An illustration of the steps of our spiral arm detection method. Top left: the unsharp, masked *B*-band image. Points were marked on this image to define the spiral arms. Top right: the unsharp, masked *B*-band image in log-polar coordinates. The different colored points and lines show the spiral arm segments that were fitted with different pitch angles. Bottom left: the masked *B*-band image with the spiral arm segments overlaid on top. Bottom right: an illustrative schematic of the morphological masks used. The black circle marks the boundary between the main and outer disk at 430″ (14.4 kpc). See text.

First, we create an unsharp mask using the *B*-band image from Mihos et al. (2013). This is done by convolving the image with a Gaussian kernel and then dividing the original image with the smooth convolved image (Malin 1977). The width of the Gaussian kernel was chosen to be 30 pixels (43$''$.5). This unsharp mask highlights the spiral features in the disk of M101. Points along each spiral arm are marked in `SAOImage ds9` (Joye & Mandel 2003), and their coordinates are then transformed into logarithmic polar coordinates, ($\ln(r)$, $\theta$), where true logarithmic spirals appear as straight lines.

It is here that we deviate slightly from previous works. To allow for the pitch angle to vary as a function of radius, we start by making a preliminary visual estimate of the arm segments in log-polar coordinates. We then pass these starting values into our code to refine the number of break points in the data. The positions of those break points are estimated iteratively using the break-fitting method outlined in Muggeo (2003) and implemented with the `Python` package `piecewise-regression` (Pilgrim 2021). The algorithm randomly generates a series of break points and fits a model of a line with a term that incorporates a change in gradient between some number of segments of a piecewise function. Using ordinary linear regression and bootstrap resampling (Wood 2001), this process is iterated until the position of the break converges. The results of this semiautomatic process are then projected back into the plane of the sky.

We then need to define a width of each of our spiral arms. Since we want to differentiate between the star-forming spiral arms and the less active interarm regions, we use the continuum-subtracted H$\alpha$ image to iteratively dilate the spiral arm until the measured H$\alpha$ flux within the arm reaches an empirical threshold following the procedure outlined in Querejeta et al. (2021). This process results in widths of 2–2.5 kpc, encompassing most of the H$\alpha$ emission that one would associate with an arm by eye.

Finally, we define the interarm regions. For simplicity, the interarm regions are simply any part of the galaxy not in the spiral arms or inner disk. This does include the extreme outer disk of M101, where there are no spiral arms but still low levels of star formation. Figure 4 shows the spiral arm and interarm masks, as well as an illustration of the process described above.

### 3.3. Main and Outer Disks

In addition to the morphological masks described above, we also make a distinction between the main and outer disks of M101. This is motivated by two reasons. First, the outer disk of M101 has structures that are quite irregular and likely tidally induced in nature, while the main disk is relatively ordered. We would then expect the outer disk to be more disorganized in terms of any stellar age gradients. Second, the high surface brightness main disk has a higher signal-to-noise ratio (S/N) than the outer disk and, unlike the outer disk, can be studied without the need for large-scale rebinning of the pixel data. While both disk regions will be analyzed in similar ways, the LSB of the outer disk requires a different treatment to build up signal.

Therefore, we define a boundary of 430″ (14.4 kpc), roughly three times the disk scale length (Mihos et al. 2013; Watkins et al. 2017). We define the main disk to be inside this boundary, including the inner disk and portions of the spiral arms and interarm regions. We define the outer disk to be outside this boundary to a radius of 920″ (30.8 kpc). The maximum radius was chosen to represent where the sky noise starts to dominate in our images. This is also approximately the outermost radius at which H II regions were detected in Garner et al. (2022).

Finally, in order to maximize the S/N in our images, we create a binned version of our narrowband images. Using the masked images, for studying the main disk, we bin the image into 9 × 9 pixel (13″ × 13″ or 450 × 450 pc) blocks, calculating the median intensity of unmasked pixels in each block. In order to quantify uncertainties for each of these blocks, we also calculate the uncertainty estimate of the median (Rider 1960; Williams 2001),

$$\sigma_{\mathrm{median}} = \sigma_{\mathrm{mean}}\sqrt{\frac{\pi}{2}} = \mathrm{std}\sqrt{\frac{\pi}{2N}}, \tag{1}$$

where std is the standard deviation, $N$ is the number of pixels in a block, and $\sigma_{\mathrm{mean}}$ is the uncertainty in the mean. However, when studying the outer disk, we bin over much larger scales, described later in Section 6. It is from these medianed blocks that we calculate fluxes and EWs in each of the environments described above. In order to further maximize the S/N, in the main disk region, we reject low-S/N pixels at a threshold that corresponds to a surface brightness of roughly $\mu_B = 23.6$ mag arcsec$^{-2}$.

## 4. Inferring Ages with Absorption Lines

To connect our measured narrowband imaging to the underlying stellar populations, we utilize the SED fitting and modeling Code Investigating GALaxy Emission (CIGALE; Noll et al. 2009; Boquien et al. 2019). To illustrate how our filters span various spectral features, Figure 5 shows the SED of an instantaneous burst of star formation with solar metallicity that evolves to late times as generated with CIGALE. Two broad spectral features are covered by our filters: individual Balmer lines in both the H$\beta$ and [O II] filters and, in the [O II] filter, the slope of the blue continuum between the Balmer break at 3646 Å and the 4000 Å break, produced primarily by A/F and O/B stars, respectively. It is important to note that we cannot make a standard $D_{4000}$ measurement, as both of our [O II] filters are bluer than the wavelengths typically used for the $D_{4000}$ measurement (Bruzual 1983; Balogh et al. 1999).

Our H$\beta$ filters are most sensitive to the strengths of their respective Balmer lines, while our [O II] filters are sensitive to the strengths of the higher-order Balmer lines and the slope of the continuum between the Balmer break and the 4000 Å break. Fortuitously, the H$\beta$ filters are positioned in such a way that they avoid measuring the nearby metallic lines, which reduces the chance of any secondary metallicity effects in the Balmer lines. On the other hand, the [O II] filters act as a sort of "pseudomeasurement" of the Balmer and 4000 Å breaks, targeting no specific feature but sensitive to all of them. This motivates the need for stellar population modeling to understand how populations of different ages, metallicities, dust absorption, etc., behave through our filters.

### 4.1. Stellar Population Parameters

In order to understand how the narrowband spectral features progress with age and what stellar population parameters they are sensitive to, we created a grid of model SFHs using CIGALE. While CIGALE is most commonly used to fit the observed multiwavelength SED of galaxies, we instead use CIGALE as a simple spectral synthesis code to model the observed EWs in each filter pair under a variety of SFHs. In this way, we can use our understanding of the models to inform our understanding of the data set. In the following, we describe the parameters that we investigated. The input parameters and their values used are listed in Table 1. CIGALE uses theoretical models to parameterize the flux emitted and absorbed by the stars, gas, and dust in model galaxies and produces a grid of model spectra that are then converted to SEDs. Boquien et al. (2019) describes the input models in complete detail, and we briefly review each chosen component and its contribution.

To build a model galaxy SED, we first need to define the properties of the underlying stellar population in terms of an assumed stellar population synthesis model, an initial mass function (IMF), and SFH. We adopt here in all models the high-resolution version of the Bruzual & Charlot (2003) stellar population synthesis models. We also adopt the Chabrier (2003) IMF with solar metallicity ($Z_{\odot} = 0.02$). While M101's average stellar metallicity is somewhat subsolar ($Z = 0.5 \pm 0.3\ Z_{\odot}$; Lin et al. 2013), the relative insensitivity of the line strengths to metallicity in our filters make this a reasonable choice. However, we do investigate the effect of subsolar ($Z = 0.008$, $0.4\ Z_{\odot}$) and supersolar ($Z = 0.05$, $2.5\ Z_{\odot}$) metallicities on the generated models in the next section.

We model the SFH as one or two decaying exponentials (Figure 6). The first exponential models the long-term star formation that has formed the underlying stellar mass of the disk, while the optional second exponential models a more recent burst of star formation as might be expected due to spiral arm passages or tidal encounters. Both exponentials are parameterized by the $e$-folding times of the old and young populations ($\tau$ and $\tau_b$, respectively), the time since the beginning of each star formation model for the old and young populations ($t$ and $t_b$, respectively), and the fraction of stars formed in the second burst relative to the total mass of stars

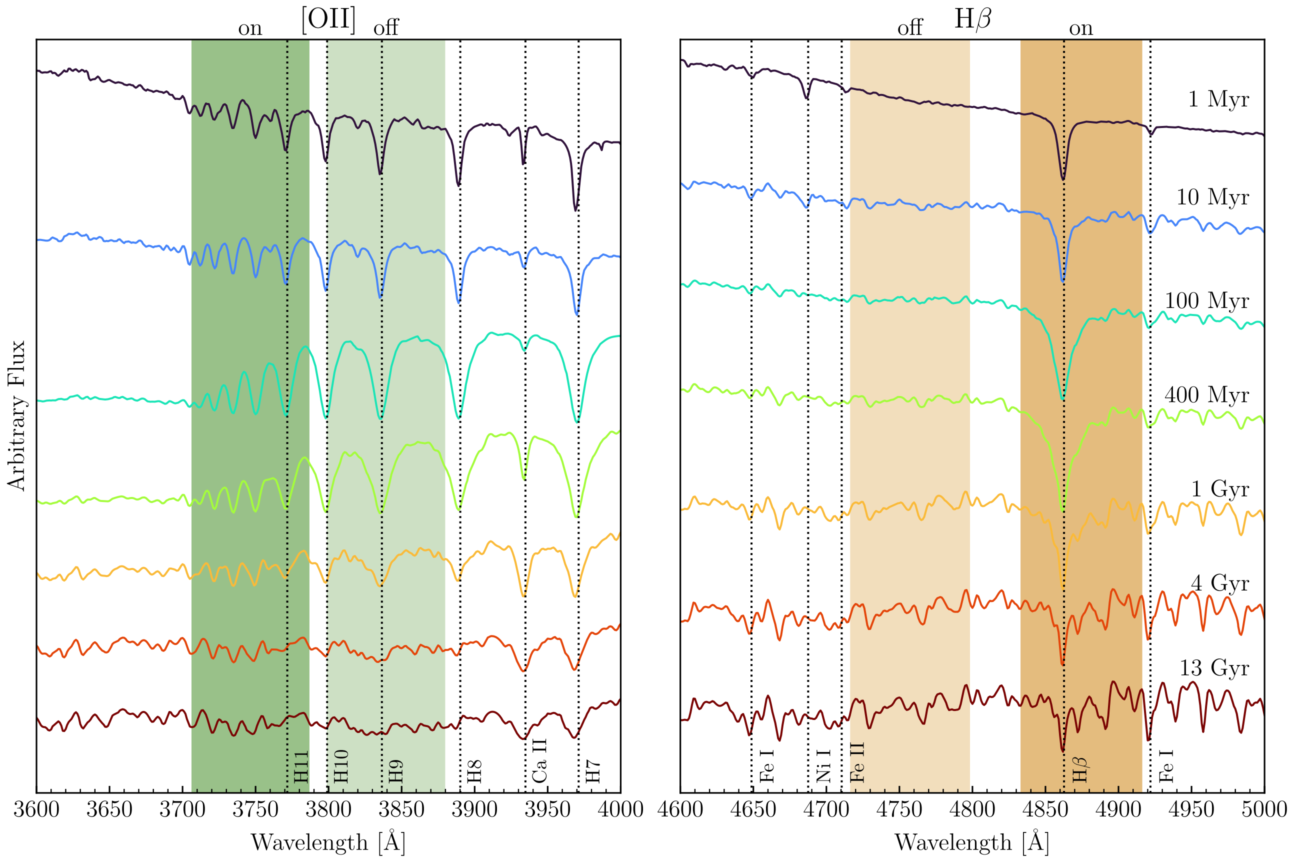

**Figure 5.** The SED of an instantaneous burst of star formation at solar metallicity and with a Chabrier (2003) IMF, increasing in age from top to bottom: 1, 10, 100, and 400 Myr and 1, 4, and 13 Gyr. Left: the [O II] filter set. Right: the H$\beta$ filter set. In both panels, the on-band is darker than the off-band. SEDs created with CIGALE (Noll et al. 2009; Boquien et al. 2019).

ever formed, $f_b$. The standard values we take for the $e$-folding times are $\tau = 30$ Gyr (i.e., mimicking a slowly declining star formation rate) and $\tau_b = 100$ Myr. For reference, under exponential SFH models, typical $e$-folding timescales for spiral galaxies range from 2 to 30 Gyr (Bolzonella 2000).

Dust attenuation is handled following the Charlot & Fall (2000) model. This model makes the distinction between the heavily extinguished stellar birth clouds and the less extinguished ambient ISM. We vary the $V$-band attenuation of the ambient ISM, which also proportionally varies the $V$-band attenuation of the stellar birth clouds (see Equation (7) in Boquien et al. 2019). For reference, Lin et al. (2013) derived an integrated, global extinction for M101 of $A_V = 0.24$, although the central region is dustier, $A_V = 0.41$ (see also Boissier et al. 2004). For our study, since we are masking the dense star-forming H II regions before analysis, we expect typical extinction values for the regions we study to be significantly lower.

### 4.2. Diagnostic $W_{3746}$ versus $W_{H\beta}$ Plots

Using these models, we perform a few basic tests to investigate to which parameters our narrowband filters are most sensitive. We calculate the EW in our H$\beta$ and [O II] filters, $W_{\mathrm{H}\beta}$ and $W_{3746}$, respectively, through all of the models.[6] Then, holding all parameters constant, we vary each parameter and see how the EWs vary as a function of that parameter in our diagnostic $W_{3746}$ versus $W_{\mathrm{H}\beta}$ plots. Figure 7 shows these plots for four different varying parameters: the $e$-folding timescale of the main population, $\tau$; the metallicity, $Z$; the age of a recent burst, $t_b$; and the $V$-band dust attenuation in the ISM, $A_{V,\mathrm{ISM}}$.

Broadly speaking, in each plot as a function of age, $W_{\mathrm{H}\beta}$ and $W_{3746}$ numerically decrease (stronger absorption in H$\beta$; less flux in the [O II]-on band than the [O II]-off band) at very young ages, $10\ \mathrm{Myr} \lesssim t \lesssim 600\ \mathrm{Myr}$. When the models reach 600 Myr ages, both EW measurements begin to numerically increase again, with $W_{\mathrm{H}\beta}$ increasing at a faster rate than $W_{3746}$. The age of 600 Myr is approximately the lifetime of an A main-sequence star, for which the Balmer absorption lines are strongest. Since our [O II] filters are heavily sensitive to the higher-order Balmer lines, this produces a similar effect in $W_{3746}$.

The top left plot of Figure 7 shows how these quantities vary as we allow the $e$-folding timescale of the main population to change. We see that regardless of the timescale, a young population will follow the same track in the diagnostic plot until reaching an age of 600 Myr. Shorter star-formation timescales (i.e., short main bursts) that are not continually replenishing their supply of A-type stars rapidly have their $W_{\mathrm{H}\beta}$ diminish. Meanwhile, as the higher-order Balmer lines give way to weak absorption lines in our [O II]-on band, molecular bands (such as CN) contributed by the dominating presence of cooler stars create large absorption features in our [O II]-off band, having the effect of creating artificial "emission" in $W_{3746}$ (i.e., $W_{3746} > 0$). In contrast, larger $e$-folding timescales (more

---

[6] We note again for clarity that $W_{3746}$ does not refer to the EW of an individual absorption line; 3746 refers only to the central wavelength of the filter.

**Table 1**
Input Parameters for SED Model Grid

| Parameter | Symbol | Range |
|---|---|---|
| IMF: Chabrier (2003) | | |
| Metallicity | $Z$ | 0.008, 0.02, 0.05 |
| Redshift | $z$ | 0.0008 |
| SFH: `sfh2exp` | | |
| Age of main population | $t$ | 0.01, 0.02, 0.03, 0.04, 0.05, 0.06, 0.07, 0.08, 0.09, 0.1, 0.15, 0.2, 0.4, 0.6, 0.8, 1, 1.2, 1.4, 1.6, 1.8, 2, 2.3, 2.5, 2.7, 2.9, 3.1, 3.5, 3.7, 3.9, 4.1, 4.3, 4.5, 4.7, 4.9, 5.1, 5.3, 5.5, 5.7, 5.9, 6.1, 6.3, 6.5, 6.7, 6.9, 7.1, 7.3, 7.6, 7.8, 8, 8.2, 8.4, 8.6, 8.8, 9, 9.2, 9.4, 9.6, 9.8, 10 Gyr |
| *e*-folding timescale of main population | $\tau$ | 0.1, 0.3, 0.5, 1, 2, 3, 4, 5, 10, 15, 20, 30 Gyr |
| Age of a recent burst | $t_b$ | 10, 50, 100, 500 Myr |
| *e*-folding timescale of recent burst | $\tau_b$ | 50 Myr |
| Burst fraction of total mass | $f_b$ | 0.0, 0.01, 0.1, 0.5, 0.7, 0.9 |
| Dust Attenuation: `dustatt_modified_CF00` | | |
| *V*-band attenuation in the ISM | $A_{V,\mathrm{ISM}}$ | 0.0, 0.1, 0.3, 0.5 |
| Fraction of total effective optical depth contributed by ISM | $\mu$ | 0.44 |
| Power-law slope of dust attenuation in the ISM | $\delta_{\mathrm{ISM}}$ | −0.7 |
| Power-law slope of dust attenuation in the birth clouds | $\delta_{\mathrm{BC}}$ | −1.3 |

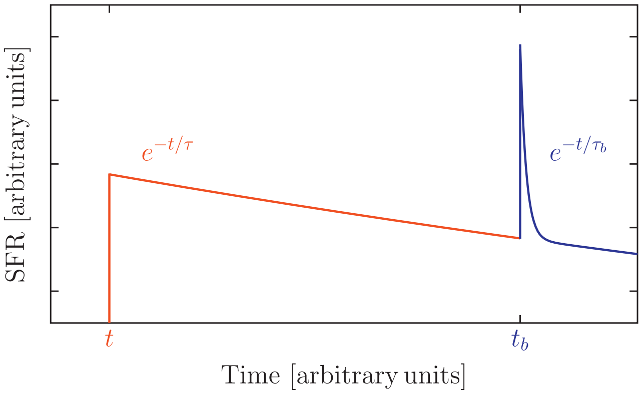

**Figure 6.** Schematic of the modeled SFHs used. Red lines and text show the main population while blue lines and text show the recent burst population. The grid samples the labeled parameters (e.g., $t$, $t_b$, $\tau$, and $\tau_b$) over reasonable ranges. See text.

constant star formation) have more young stars at late times, which result in more absorption in the Balmer lines, resulting in more negative EWs in both filters even at late times.

Adjusting the metallicity of the stellar populations (top right of Figure 7), we see that the strengths of $W_{\mathrm{H}\beta}$ and $W_{3746}$ change in well-understood ways (e.g., González Delgado et al. 1999, 2005). At ages younger than 1 Gyr, the strength of the Balmer lines has only a small dependence on metallicity caused by the dependence of stellar evolution in the integrated light of a stellar population. Again, the stellar metallicity of M101 is slightly subsolar (Lin et al. 2013), but the subsolar and solar metallicity tracks greatly differ only for very young ages, $\lesssim$100 Myr. At ages older than 1 Gyr, the Balmer line metallicity dependence is stronger. Again, in addition to the higher-order Balmer lines, the $W_{3746}$ measure also feels the increasing effect of molecular bands at old ages, which are slightly elevated at higher metallicities.

Allowing for a recent burst of star formation (bottom left of Figure 7) creates strong variations in the strengths of $W_{3746}$ and $W_{\mathrm{H}\beta}$. In these models, the main population is always older than the burst population. It is clear that very recent bursts dominate the light from the old population and approach the characteristics of a population dominated by younger stars. This is primarily attributed to the addition of more A-type stars, deepening the Balmer lines, leading to stronger signatures in $W_{3746}$ and $W_{\mathrm{H}\beta}$.

Finally, including the effects of dust attenuation in the ISM can affect the EWs, particularly at young ages, when stars are presumed to be in their birth clouds (bottom right of Figure 7). The effect on $W_{\mathrm{H}\beta}$ is strongest for young ages, where dust greatly weakens the strength of the absorption line. In the models of Charlot & Fall (2000), young stars are embedded in heavily extinguished birth clouds in addition to the dust in the ISM leading to the absorption line weakening we see for young ages. Since all Balmer lines are plagued by this effect to some degree, we see a similar but smaller trend in $W_{3746}$. At old ages, the Balmer lines are slowly becoming weaker, while age-independent molecular bands start to contribute, keeping the $W_{3746}$ relatively constant. Both of these trends are explored in more detail by MacArthur (2005) in the context of the Lick indices and $D_{4000}$ measurements.

Briefly summarizing the models, we see that we are very sensitive to some physical properties while being relatively insensitive to others. Among those that we are most sensitive to are differences between the *e*-folding timescales of the main population and recent bursts of star formation. As we will discuss in the next section, recent bursts may explain stellar populations that lie in between the two "prongs" predicted by the main population. We are less sensitive to the effects of metallicity and dust. Both are constrained by previous measurements (Boissier et al. 2004; Lin et al. 2013), although dust may have a similar scattering effect to a recent burst of star formation where any local dustier regions might artificially weaken the absorption lines we measure. Again, however, since we have masked the youngest, dustiest regions of M101—the star-forming H II regions—these effects should be relatively small.

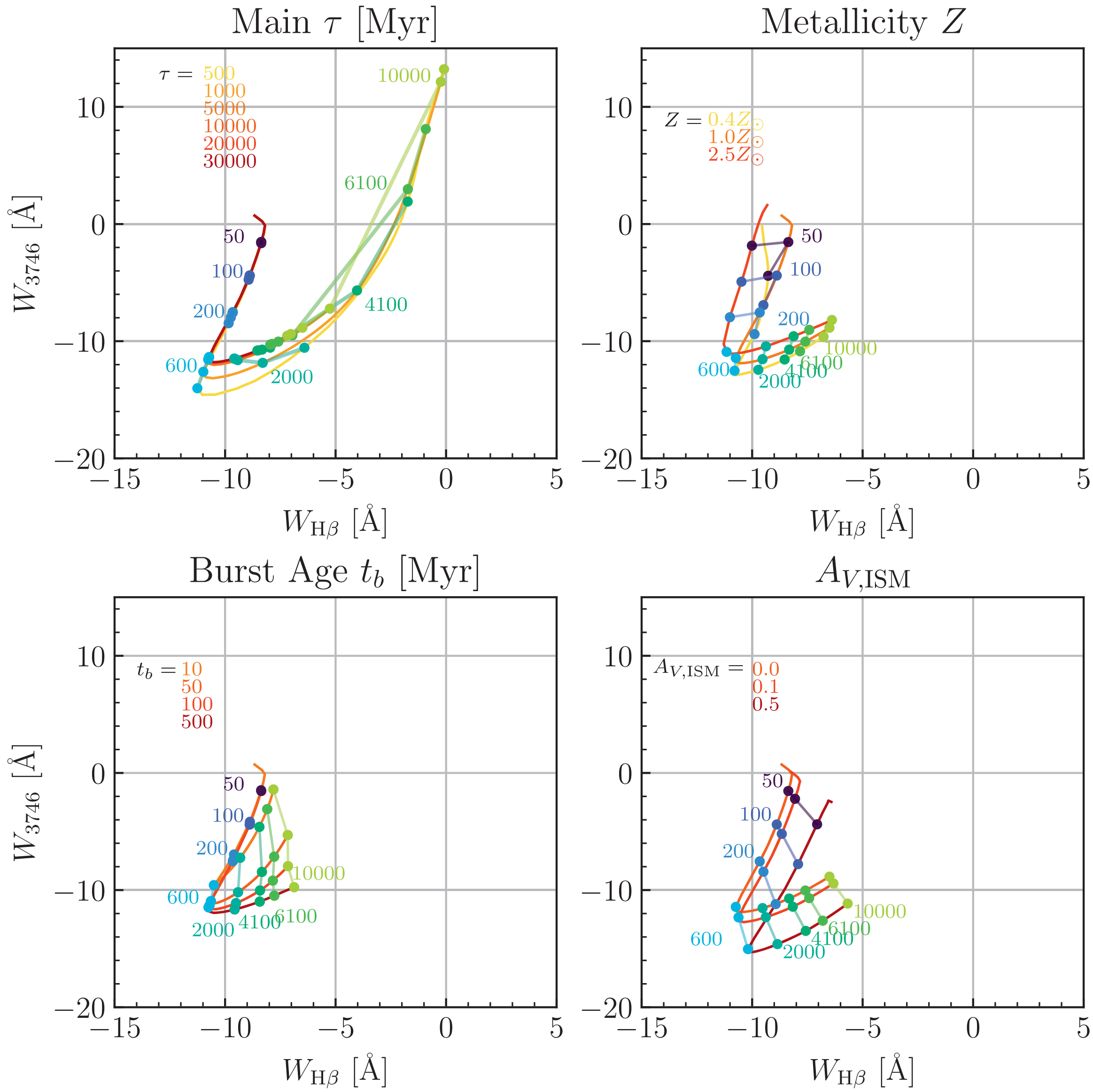

**Figure 7.** Models for $W_{3746}$ vs. $W_{\mathrm{H}\beta}$ under different parameter assumptions using CIGALE. Strong absorption is to the bottom left in each plot. All models assume a Chabrier (2003) IMF. Colored points along each track indicate the age of the population in Myr. Top left: varying the main population $\tau$, assuming solar metallicity and no recent burst. Top right: varying the metallicity, assuming $\tau = 10$ Gyr and no recent burst. Bottom left: varying the burst age, assuming solar metallicity, $\tau = 10$ Gyr, $\tau_b = 100$ Myr, and $f_b = 1\%$. Bottom right: varying the dust attenuation, assuming solar metallicity, $\tau = 10$ Gyr, and no recent burst.

## 5. The Stellar Ages of the Main Disk

In this section, we begin by comparing the stellar population models generated with CIGALE to the binned data inside the main disk (including what we have defined as the inner disk) to investigate any broad age trends present. Then, we examine how the stellar population ages differ between different environments, namely, between the spiral arms and interarm regions. As a reminder, we define the main disk of M101 to be those regions inside 430″ (14.4 kpc) of the center (Section 3).

Figure 8 shows our diagnostic $W_{3746}$ versus $W_{\mathrm{H}\beta}$ plot for those binned pixels in the main disk of M101 colored by radial distance from the center. Also shown is the prediction from CIGALE models of where different SFHs should fall on this plot. Here, the colored lines show different SFH models assuming different *e*-folding times of the main stellar population, ranging from 500 Myr in light orange to 10 Gyr in red. Points along the tracks are labeled by the age of each model along the track. These models also include the effects of dust assuming an average value of $A_{V,\mathrm{ISM}} = 0.3$ (Lin et al. 2013).

Comparing the data with the generated models generally shows that the inner regions within a few kiloparsecs are consistent with an older stellar population, while the mean age generally becomes younger at larger radii. This is more easily seen in the right panel of Figure 8, where we plot three radial ranges with density contours. Thus, we see that those points at large radii are truly younger, with very few old populations mixed in, and vice versa for the points at small radii. Thus, we recover a radial age gradient for the main disk of M101.

We also see that the two “prongs” of the models can be loosely considered the bounds of “reasonable” stellar populations. However, a small number of points scatter well outside the model tracks: one plume at high $W_{3746}$ and $W_{\mathrm{H}\beta} \sim -5$ Å and another at high $W_{\mathrm{H}\beta}$ and $W_{3746} \sim -5$ Å, and a large population of points between the two “prongs”. Investigating

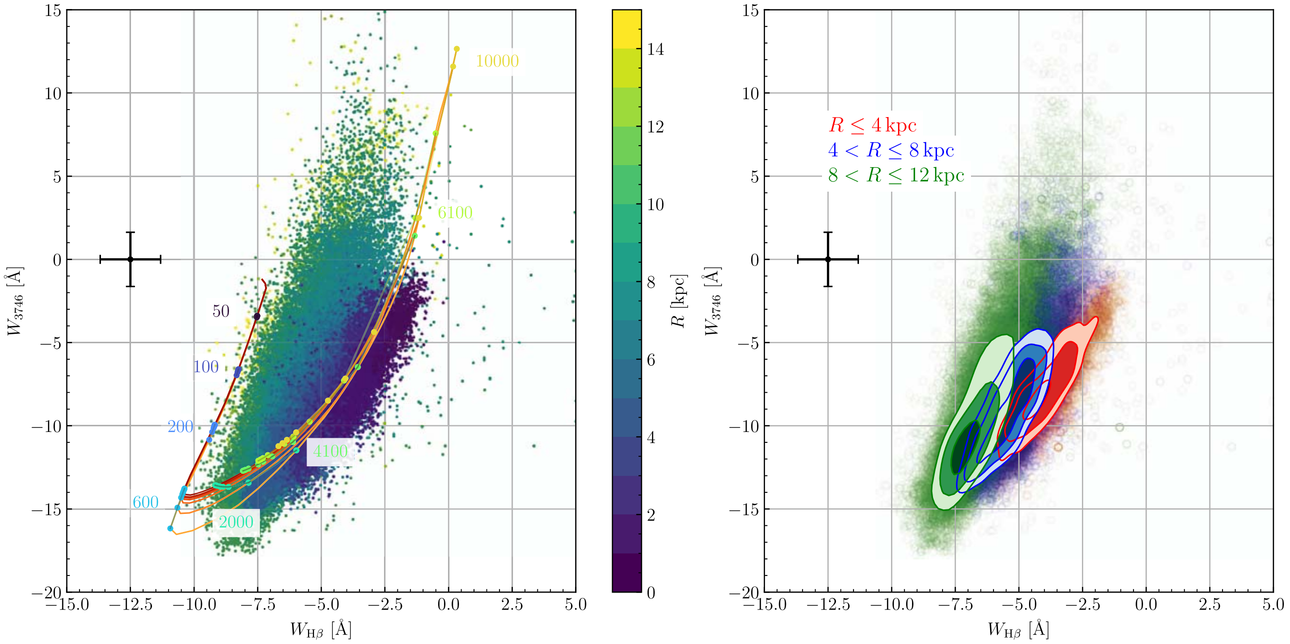

**Figure 8.** $W_{3746}$ vs. $W_{\mathrm{H}\beta}$ for all medianed pixels in the main disk of M101 ($R < 430''$, ~15 kpc). Left: points are colored by distance from the center of M101. The standard uncertainty is shown in the upper left. Overplotted are different models from CIGALE. Models assume a Chabrier (2003) IMF, solar metallicity, and $A_{V,\mathrm{ISM}} = 0.3$. Different colored lines indicate different $\tau$ models: 0.5, 1 , 2, 3, 4, 5, and 10 Gyr. Ages of the stellar populations are indicated on the plot. Right: contours are colored by distance from the center of M101: $R \leqslant 4$ kpc in red, 4 kpc $< R \leqslant 8$ kpc in green, and 8 kpc $< R \leqslant 12$ kpc in blue. Characteristic error bars are shown in the top left. Contours show the data point density for different radial ranges, encompassing 30%, 50%, and 80% of all data points in each range.

the locations of the two plumes on our images shows that these are caused by either an unmasked foreground star or scattered diffuse light from masked H II regions.

Most of the true scatter lies between the two prongs of the model. Returning to Figure 7, we see that the effect of a recent burst is to bend the older prong inward toward the younger prong. As mentioned before, this can be physically attributed to the addition of A-type stars, deepening the Balmer absorption lines. The addition of O/B stars will also weaken the slope of the blue continuum, increasing the value of $W_{3746}$ despite there also being a host of A-type stars as well. Therefore, recent bursts will move stellar populations slightly away from the bend in the prongs in our models.

There are also a large number of points "in emission" in $W_{3746}$ in Figure 8. As mentioned previously (Section 4.2), this is not caused by any real emission feature being measured but rather flattening continuum levels in our [O II] filters combined with molecular bands such as CN appearing in our [O II] off-band filter, creating a false "emission" measurement. Recent bursts will bend the older prong inward toward being "in absorption" in $W_{3746}$ caused by the presence of A-type stars. Given the globally constant and locally stochastic star-forming nature of spiral galaxies, we then expect that pixels dominated by old populations but with a somewhat recent burst (i.e., $t_b \sim 500$ Myr) will populate this area characterized by being "in emission" in $W_{3746}$.

### 5.1. Inner Disk versus Arm versus Interarm

We now turn our attention to how the different main disk environments (inner disk, spiral arms, and interarm) are spectrally distinct. Applying the masks described in Section 3, Figure 9 shows how these environments distribute themselves on our $W_{3746}$ versus $W_{\mathrm{H}\beta}$ plot. Here, each environment is shown in a different color with density contours overlaid. The inner disk has a tendency to separate itself from the more actively star-forming spiral arms and interarm regions. Notably, there is also a distinct offset between the centroids of the density distributions for the spiral arms and interarm regions.

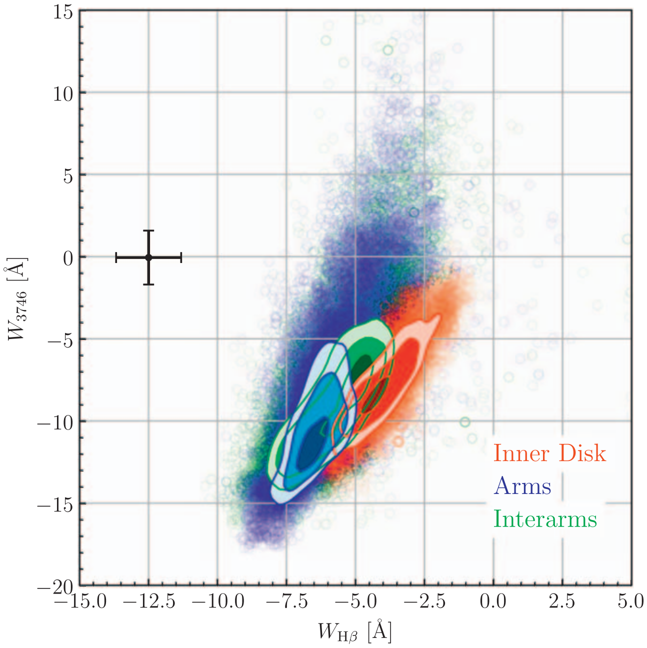

**Figure 9.** $W_{3746}$ vs. $W_{\mathrm{H}\beta}$ for all pixels in the main disk of M101 ($R < 430''$, ~15 kpc) distinguished by environment: the inner disk in red, spiral arms in blue, and interarm regions in green. Characteristic error bars are shown in the bottom right. Contours show the data point density for different environments, encompassing 30%, 50%, and 80% of all data points in each category.

These differences, just as in Figure 8, can be broadly interpreted as age differences: the inner disk has a stellar

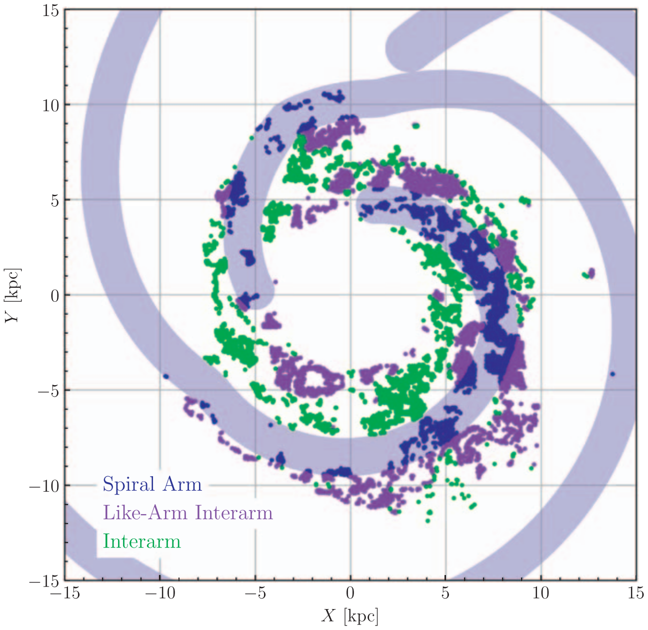

**Figure 10.** The spatial distribution of spectrally selected regions (see text). The points labeled "interarm" are those that are spectrally distinct from the spiral arms, while those labeled "like-arm interarm" are those that are spectrally indistinct from the spiral arms. The schematics of the spiral arms are the light blue regions.

population that is older than that in more actively star-forming arm and interarm regions. However, it is worth mentioning that what we define to be the inner disk is much larger than is traditional, since we defined the inner disk based on the inability to discern separate spiral arms. This might cause smaller changes in the stellar ages to be unresolvable. For instance, Lin et al. (2013) found that the bulge of M101 ($R \lesssim 20''$) has a younger stellar age than the surrounding disk by ∼3 Gyr using pixel-based multiwavelength SED fitting. Young bulges are found in numerous late-type galaxies (e.g., Ganda et al. 2007; Peletier et al. 2007), and M101 does have a mildly star-forming pseudobulge (Fisher et al. 2009; Fisher & Drory 2010; Kormendy et al. 2010). However, given the extensive network of H II regions in the inner kpc of M101, this region is largely masked in our imaging and thus not measured by our analysis.

Moving on to the spiral arms and interarm regions, the spiral arms are dominated by a recently formed young population, while the interarm region is slightly mixed in ages. The interarm has a sizable young population that overlaps with the spiral arm distribution but also stellar populations that have an older mean age, more similar to the non-star-forming populations of the inner disk. The observation that the interarm region has a mix of different stellar populations prompts the question of if these populations are spatially distinct.

To test this, we select two spectral regions on our diagnostic plot. We select interarm points that are spectrally distinct from the majority of the arm points, that is, $-5\,\text{Å} \leqslant W_{\mathrm{H}\beta} \leqslant -4\,\text{Å}$ and $-7\,\text{Å} \leqslant W_{3746} \leqslant -5\,\text{Å}$, and arm and interarm points that are spectrally indistinguishable, that is, $-7\,\text{Å} \leqslant W_{\mathrm{H}\beta} \leqslant -6\,\text{Å}$ and $-13\,\text{Å} \leqslant W_{3746} \leqslant -10\,\text{Å}$. These points are located approximately where the densest contours lie in Figure 9. Thus, the interarm region is split into "like-arm" interarm regions and "true" interarm regions, defined by their spectral properties. Figure 10 shows the spatial distribution of these spectrally defined regions.

What is immediately apparent is that the like-arm interarm regions are preferentially found on the outer edge of the spiral arm, while the true interarm regions are found on the inner edge of the spiral arm. According to our stellar population models, the spiral arm and like-arm interarm regions have similar stellar ages, while the true interarm regions are older. Thus, we observe a potential age gradient in the ages of stars across a spiral arm. There are small areas of like-arm interarm regions that appear to be continuations of a spiral arm, particularly toward the inner disk. This feature is likely caused by the difficulty of defining spiral arms in such a tightly wound environment.

While Figure 10 shows the spatial distribution of points selected by their spectral characteristics, an alternative analysis is to look at the spectral characteristics of points along a track cutting through the spiral arms. To check this, in Figure 11, we select three rectangular regions extending from outside the inner disk environment, extending through one spiral arm, and ending about halfway to the next spiral arm (i.e., in the middle of an interarm environment). Investigating the trend of $W_{\mathrm{H}\beta}$ with distance across a spiral arm, we see the expected age characteristics: inside the arm lies weak absorption produced by older stellar populations, while moving outside the arm is associated with the strengthening absorption of younger stellar populations. Clearly these conclusions are supported not only by the SFH modeling as in Figure 10 but also observationally with direct measurements of the age-sensitive $W_{\mathrm{H}\beta}$ as in Figure 11.

Interpreting these observed age trends in the context of spiral density waves is relatively straightforward due to the ordered nature of the main disk of M101. These age trends are well described by the large-scale shock scenario (Roberts 1969; Dixon 1971), which predicts that inside of corotation, ages should change along these cuts through the arm, in this case decreasing along our chosen direction. Thus, our observations give strong support for the dynamical scenario where the main disk is characterized by a quasi-steady global spiral wave. As mentioned in the Introduction, this age trend is often hard to measure due to the use of broadband colors and the well-known age–metallicity degeneracy. However, techniques that control for the reddening effects of dust and metallicity, such as the optical/infrared photometric index used by González & Graham (1996) and Martínez-García et al. (2009), have started to reveal these age trends across spiral arms.

Similarly in our data, our ability to detect these age differences may be due to the reduced sensitivity to dust and metallicity in our narrowband imaging compared to broadband optical studies. As mentioned earlier (Section 4.2), $W_{3746}$ and $W_{\mathrm{H}\beta}$ have different responses to dust and metallicity; $W_{\mathrm{H}\beta}$ is only sensitive to one Balmer line that strongly weakens for older populations, while $W_{3746}$ is sensitive to many Balmer lines and the shape of the blue continuum, which strongly weakens for younger populations. The combination of these two age indicators allows us to break the degeneracies any one indicator might have (MacArthur 2005).

## 6. The Stellar Ages of the Outer Disk

Studying the stellar component of the galaxy outskirts is particularly challenging. The surface brightness of the outer stellar component is usually well below that of the night sky,

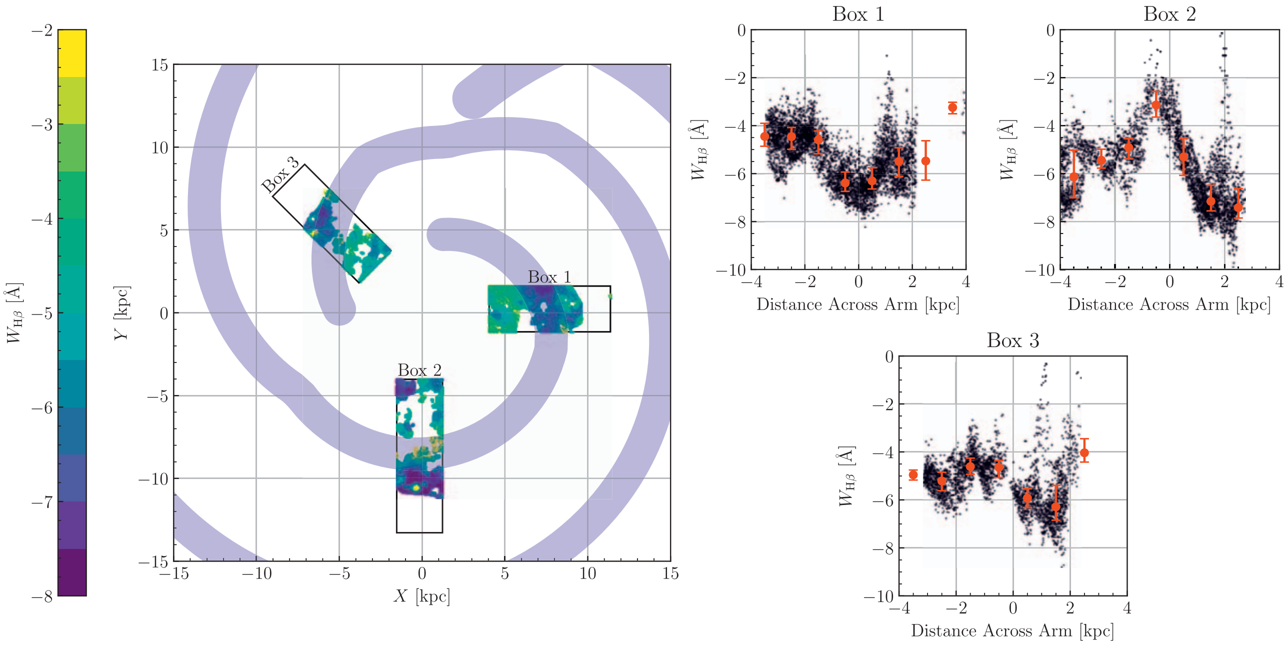

**Figure 11.** The spectral characteristics of spatially selected regions. Left: three selected boxes in the main disk. Points are colored by their $W_{H\beta}$. Empty regions in the boxes are either caused by masked H II regions or are below our S/N cut. Right: each box's $W_{H\beta}$ as a function of distance across a spiral arm. Negative distances are toward the center of M101, and positive distances are away from the center of M101. Binned medians are shown in red. In all three boxes, the $W_{H\beta}$ is stronger on the outer edge of an arm ($1 \lesssim X \lesssim 3$) than the inside of the arm ($-3 \lesssim X \lesssim -1$), indicative of the shift toward younger populations ahead (moving out of) the arm.

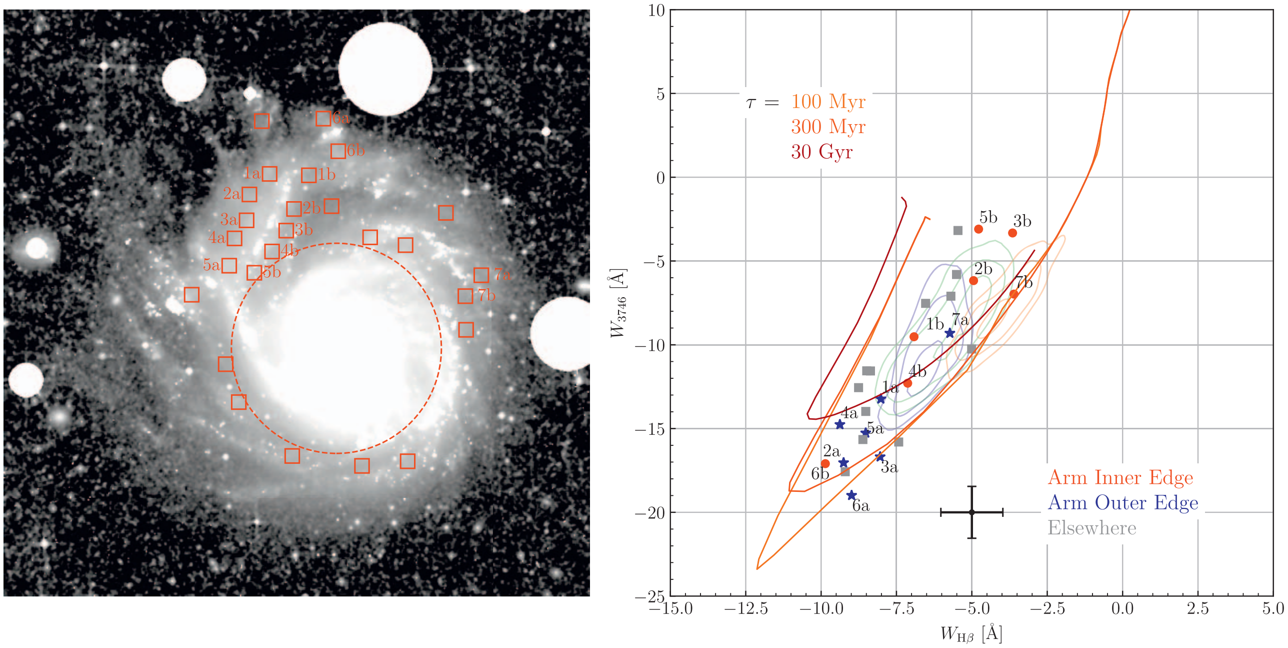

**Figure 12.** Left: the median binned H$\beta$ off-band image of M101. H II regions and foreground stars are masked. The red dashed circle marks the main/outer disk distinction, $R = 430''$. Selected regions in the outer disk are marked by red boxes measuring 40 × 40 pixels (58″ × 58″ or 2 kpc × 2 kpc) and numbered. The image measures 40′ × 40′ or 80 kpc × 80 kpc. North is up, and east is to the left. Right: the selected regions' distribution on the diagnostic plot. Labels are carried over from the left panel. Colored points and text (lower right) correspond to the different environments of the regions selected. The colored contours correspond to the density distribution of different environments in the main disk, same as Figure 9. Colored tracks and text (upper left) correspond to different SFHs with different $\tau$. Characteristic error bars are shown in black at the bottom right.

requiring very deep and accurate photometry to constrain the properties of the stellar populations (e.g., Mihos et al. 2013; Watkins et al. 2016; Peters et al. 2017). In addition, the LSB outer regions can be contaminated by background sources and instrumental scattered light, complicating the measurement of photometric EWs. To alleviate these issues, in our analysis of the outer disk, we focus on a small sample of relatively "clean" regions in the outer disk and compare their properties and distribution to the main disk. These regions were picked by eye, marking areas that are free of contamination and have high enough surface brightness to be well detected in our narrowband imaging. Each region measures 40 × 40 pixels (58″ × 58″ or 2 kpc × 2 kpc), in which we measure the median $W_{3746}$ and $W_{H\beta}$.

Figure 12 shows the location of each region in the 9 × 9 median H$\beta$ off-band image. Particular pairs of regions inside (“a”) and outside (“b”) spiral arms are labeled. Regions 1–5 lie along the northeastern arm, chosen to sample stellar populations in the direction of the NE Plume (Mihos et al. 2013). Regions 6a and 6b sample either side of a star-forming region, and regions 7a and 7b sample the edge of a short spiral arm to the northwest. Other regions have been placed targeting interarm regions, star-forming complexes, and the faint, outer reaches of the galaxy. In this way, we have attempted to target different features in M101’s outer disk while also remaining azimuthally unbiased.

Figure 12 also shows these regions’ locations on the diagnostic $W_{3746}$ versus $W_{\mathrm{H}\beta}$ plot. Comparing these outer disk regions with the main disk environments, we see that while there is overlap, many regions show stronger absorption features in one or both of our filters than the main disk. Notably, many of these regions are those that are along the northeast arm. Stronger absorption is indicative of a more dominant young population than that in the main disk, suggesting recent star formation in these regions perhaps as a result of the M101–NGC 5474 interaction. Similar studies using broadband colors have also inferred younger ages in the outer disk (Bianchi et al. 2005; Lin et al. 2013; Mihos et al. 2013).

Also shown in Figure 12 are three representative SFH tracks generated with CIGALE. All assume a Chabrier (2003) IMF, solar metallicity, and $A_{V,\mathrm{ISM}} = 0.5$ and differ in the $e$-folding timescale, $\tau$, being 100 Myr, 300 Myr, or 30 Gyr. These are single-exponential SFHs meant to describe the bulk of the stellar population; i.e., the $\tau = 100$ Myr model approximates a stellar population that had most of its star formation early and is fading out. The effect of a shorter $\tau$, i.e., a “burstier” SFH, is to produce stronger absorption lines at the turnaround age of ∼600 Myr. The different tracks rejoin one another at late times (several gigayears).

Comparing the selected outer disk regions with these SFH tracks, we see that none of them appear consistent with the “burstiest” model, that with $\tau = 100$ Myr, suggesting a slightly more extended SFH. Meanwhile, many of the regions on the north and northeastern side of M101 are consistent with young populations. For instance, several regions could be young populations associated with a fading burst (among them regions 2a, 3a, 6a, and 6b). Others might be young populations in a near-constant SFH or a fading burst (among them regions 4a and 5a).

Interesting to note are the regions in the direction of the NE Plume beyond the northeast arm (regions “a” 1–5). These five regions form a tight cluster of points in Figure 12, near the turnaround point in the SFH tracks. The fact that they have strong absorption features through our filters suggests that these are young ages, consistent with a recent (few hundred Myr) burst of star formation on top of a somewhat older but not dominant background stellar population. This timescale is similar to that found by Mihos et al. (2018), who used HST to study the discrete stellar populations in M101’s NE Plume (at a slightly larger radius than probed here), finding evidence for both an old population and a ∼300 Myr starburst population in the region. In our studies of the integrated light here, the starburst population and older background populations combine to give an older mean age (500 Myr–1 Gyr), but the scattering of regions shows good agreement with the picture of a recent weak starburst in this part of M101’s outer disk.

However, Figure 12 also shows other regions in M101’s outer disk that are dominated by older populations. Some of these lie in interarm regions or to the west of M101, a part that likely did not participate strongly in the M101–NGC 5474 interaction (in the model of Linden & Mihos 2022, these regions were on the opposite side from the companion at closest approach). Interestingly, most of the selected regions on the inside of the spiral arms (labeled “b” in Figure 12) have weaker absorption features, suggesting an older mean age than their partners on the outside of the spiral arms. These age patterns across the outer arms are similar to those seen in the main disk, again indicative of the large-scale shock scenario. However, here we are sampling regions well outside the corotation radius of the main disk (found to be at 15.6 ± 2.2 kpc; Roberts et al. 1975; Scarano & Lépine 2013). Outside of corotation, we would expect the age gradients to be flipped (older populations leading the arms and younger populations inside; Roberts 1969; Dixon 1971). The fact that we observe no change in the directionality of the age gradients in the outer arms hints at the possibility of multiple pattern speeds in M101, which we explore below.

## 7. Multiple Pattern Speeds of M101?

In the past two sections, we have presented evidence of the large-scale shock scenario in both the main and outer disks of M101. There exist age gradients across the spiral arms of M101 going from primarily old populations on the inner edge to younger populations along the outer edge of an arm. This gradient is predicted by the large-scale shock scenario (Roberts 1969; Dixon 1971), but interestingly, we see no reversal of the gradient outside M101’s main corotation radius ($R \approx 15$ kpc; Scarano & Lépine 2013), contrary to the expectation in the large-scale shock scenario.

Thus, there are two possible responses: either star formation patterns in M101 are not governed by the large-scale shock scenario or there exist multiple pattern speeds, and thus multiple corotation radii, producing the trends we observe. The large-scale shock scenario requires star formation to occur preferentially in the spiral arms, producing age gradients across the arms that flip direction inside and outside corotation. Conversely, if star formation occurs stochastically throughout the disk regardless of the location of the spiral arms, this could introduce spurious patterns in the age distributions that are inconsistent with the large-scale shock scenario. While some studies have questioned the importance of spiral arms in driving star formation (Foyle et al. 2010, 2011; Ragan et al. 2018; Querejeta et al. 2021), that does not appear to be the case in M101. Not only do we see here the gradients predicted by large-scale shocks, studies of the galaxy’s massive star populations show strongly enhanced star formation in the spiral arms (up to 30 times more efficient than in the interarm regions; Cedrés et al. 2013). This picture of spiral-driven star formation is echoed in studies of other spiral galaxies (Vogel et al. 1988; Lord & Young 1990; Knapen & Beckman 1996), and thus, at least for M101, the large-scale shock scenario likely still holds.

Instead, what is more probable is that M101 is a spiral galaxy with multiple pattern speeds. The existence of multiple pattern speeds that dominate over concentric radial ranges has been measured for M101 and other galaxies in the past. Meidt et al. (2009) used H I and CO data cubes of M101 to measure these pattern speeds and found at least three distinct speeds, each with their own corotation radius: an inner pattern within 6 kpc, a second extending from 6 to 13 kpc, and a third from 13 to 20 kpc. Each pattern has its own corotation radius: 3.7, 9.8, and 19.6 kpc, respectively. Using different methods, other studies have confirmed the innermost pattern speed as well (Egusa et al. 2009; Cedrés et al. 2013).

The possible existence of three pattern speeds in M101 could explain the recurrence of the same age trend in the outer disk as in the inner disk. At any particular radii in M101, the gas and stars would always be inside of some corotation radius, resulting in stellar populations that are primarily old along the inner edge of a spiral arm and becoming younger across the arm toward the outer edge. There would likely not be a flipping of this trend until beyond the outermost pattern speed. The fact that we do not see this flip in the outer disk of M101 does suggest that the outermost pattern speed in Meidt et al. (2009) does extend further than their cutoff of ∼20 kpc, potentially to at least 25.5 kpc (the galactocentric distance to region 1a in Figure 12).

The adoption of multiple pattern speeds necessarily requires the adoption of "dynamic" spiral arms (i.e., transient and recurrent spiral arms; e.g., Sellwood & Carlberg 1984; Elmegreen & Elmegreen 1986; Sellwood 2011) as opposed to quasi-static, long-lived spiral arms (e.g., Lin & Shu 1964; Bertin et al. 1989). In the former theory, spiral arms appear and reappear in cycles, breaking up into smaller segments with sizes of a few kiloparsecs, then reconnecting by differential rotation to reform large-scale patterns (Wada et al. 2011). Thus, dynamic spiral arms can appear to be long-lived visually but change on short timescales.

A dynamic M101 naturally has consequences for its shape and spiral structure. Multiple pattern speeds are linked and supported by "mode coupling" (Sygnet et al. 1988; Masset & Tagger 1997; see Sellwood & Carlberg 2019 and references therein for more recent discussions), wherein resonances of different pattern speeds overlap, such as the corotation radius of an inner pattern overlapping with the inner Lindblad resonance of an outer pattern. This overlap causes energy and angular momentum to be transferred efficiently to the outer disk, building up the spiral pattern at large radii (e.g., Masset & Tagger 1997; Rautiainen & Salo 1999; Meidt et al. 2008a, 2008b; Font et al. 2014). A consequence of mode coupling noted in simulations is that galaxies are stimulated to produce $m = 1$ spiral waves (e.g., Sellwood & Sparke 1988; Rautiainen & Salo 1999; Salo & Laurikainen 2000), just as we see with the large asymmetric spiral arm in M101. Notably, this might be a potential solution to the problem Linden & Mihos (2022) faced in constraining the mass of NGC 5474, having to adopt a mass ratio of one-eighth that of M101 leading to a significantly higher circular velocity for the satellite than observed in order to reproduce the asymmetry by interaction alone. If the disk of M101 was already sensitive to producing $m = 1$ modes, it could be quite responsive to tidal forcing even with a lower mass for NGC 5474. Fully hydrodynamical simulations of the M101–NGC 5474 interaction, building on the work of Linden & Mihos (2022), will need to be performed to test this theory.

However, a dynamic M101 and our measurements of an age gradient across spiral arms has consequences for computational studies of spiral structure in disk galaxies. In contrast to the canonical density wave model for spiral structure, many hydrodynamical simulations show spiral patterns forming as shearing arms that corotate with the stars and gas (e.g., Dobbs & Pringle 2010; Grand et al. 2012; Baba et al. 2015, 2017; Dobbs et al. 2017). This corotation makes it such that molecular clouds, H II regions, and star clusters do not easily move across and out of the spiral arms, predicting that no age gradients should be seen across the arm, in contrast to what we observe in M101. Other models generate spiral structure via a force response to mass clumps in the disk (D'Onghia et al. 2013; see also the introduction of Sellwood & Carlberg 2019), which produce "wakes" that extend over a small radial range and could produce the age gradients we see in M101. However, these wakes do not extend over large radii and thus do not get far from corotation. Such a model would thus predict much milder age gradients across the arms, possibly at odds with the strong age gradients we see in M101. However, we also note that most simulations of dynamic spiral arm mechanisms produce relatively weak spiral structure (e.g., Dobbs & Pringle 2010; Grand et al. 2012; D'Onghia et al. 2013). These models may provide good descriptions of "flocculent" spiral structure, but in stark contrast stands M101, a galaxy with strong spiral arms that are dynamic in nature and also likely influenced by M101's recent interaction with NGC 5474. Clearly, new simulations of dynamic spiral structure are needed that reproduce the strong spiral arms of M101 while also resulting in age gradients observed across its spiral arms.

## 8. Conclusions

Using narrowband filters that measure the absorption line strengths of H$\beta$ and higher-order Balmer lines and metallic lines between the Balmer break at 3646 Å and the 4000 Å break, we have placed constraints on the stellar ages throughout the disk of M101. We calibrate and confirm the efficacy of this technique using the stellar population synthesis code CIGALE (Noll et al. 2009; Boquien et al. 2019) to observe the effect of stellar population parameters on EWs measured through our filters. Our narrowband imaging technique proves sensitive to the SFH of the stellar populations and is only modestly sensitive to other effects, such as dust and metallicity. We divided M101 into several different radial regions to study the mean population age and also examined the differences between spiral arms and their interarm environments. We confirm studies of the overall radial age gradient, as well as show new evidence for spiral-driven features in the spatial age distribution. We interpret these results in the context of spiral arm dynamics and multiple pattern speeds in the disk of M101. Our main conclusions are summarized below.

1. In the main disk, we focused on the differences between morphological features, i.e., spiral arms, interarm regions, and the inner disk. We confirm previous studies showing a radial age gradient (Bianchi et al. 2005; Lin et al. 2013), where the inner disk has populations older than those at larger radii. Comparing spiral arms and interarm populations revealed a spread in the mean ages of the interarm population, some similar to the young arms and others older and more akin to the inner disk. These "like-arm" interarm regions are preferentially found on the outer edge of a spiral arm, while the "true" interarm regions are found on the inner edge.

2. We interpreted these spatial trends in the context of the "large-scale shock scenario" (Roberts 1969; Dixon 1971), a consequence of quasi-steady, global spiral density waves. Inside of corotation, gas clouds overtake the spiral arm and form stars in H II regions. These stars drift outward, creating a color and age gradient across the spiral arms. Despite being historically hard to measure observationally, this evolutionary path has been predicted in simulations (e.g., Dobbs & Pringle 2010) and is now clearly in evidence in our narrowband imaging.
3. To combat the low S/N in the diffuse outer disk, we selected a number of "clean" regions where we can spatially bin over larger areas to accurately measure stellar absorption signatures. Unexpectedly, we recovered a similar age trend across the spiral arms in the outer disk as we had found in the main disk, with younger populations along the outer edge and older populations along the inner edge of the spiral arms. The outer disk, while having significantly younger populations than the main disk, also contained some old populations similar to the main disk.
4. In terms of processes shaping the outer disk, the lack of a change in the spiral arm age trends beyond the assumed corotation radius of M101 suggests that there are multiple pattern speeds and thus multiple corotation radii in M101. Other groups have found evidence for radially varying pattern speeds in M101 and other galaxies (Meidt et al. 2009; Font et al. 2014), and our work supports this conclusion.

Overall, our results are consistent with a picture where M101 is a "dynamic" galaxy, one with transient and recurrent spiral arms. While still showing the radial signs expected by inside-out galaxy formation, where the inner region is older and the outer region is younger, the nature of the spiral pattern does not conform to standard density wave theory as measured by stellar ages. Instead, there may be multiple pattern speeds in M101 linked by mode coupling. This allows resonances in the different spiral patterns to overlap, causing energy and angular momentum to be transferred efficiently to the outer disk, building up the spiral pattern and resulting in the one-armed spiral pattern we see in M101. While this has promising answers for the trends in M101 seen here and elsewhere, hydrodynamical modeling of M101 and its interaction history needs to be performed to fully unravel these mysteries.

## Acknowledgments

The authors would like to thank Aaron Watkins for his work in collecting the H$\alpha$ image used for determining the widths of the spiral arms. We thank Stacy McGaugh for helpful discussions and comments on this paper. We also thank Charley Knox for his work supporting the Burrell Schmidt, and the Mt. Cuba Astronomical Society for financial support for the project. We also thank the anonymous referee for a detailed report that helped improve this paper. R.G. was supported in part by a Towson Memorial Scholarship. R.G. would like to thank STACKOVERFLOW user `ImportanceOfBeingErnest` for their `Python` code used in drawing the spiral arm masks. This publication makes use of data products from the Two Micron All Sky Survey, which is a joint project of the University of Massachusetts and the Infrared Processing and Analysis Center/California Institute of Technology, funded by the National Aeronautics and Space Administration and the National Science Foundation. This research has made use of the NASA/IPAC Extragalactic Database, which is funded by the National Aeronautics and Space Administration and operated by the California Institute of Technology.

*Facility:* CWRU:Schmidt.

*Software:* `Astropy` (Astropy Collaboration et al. 2013, 2018), `Matplotlib` (Hunter 2007), `NumPy` (Harris et al. 2020), CIGALE (Noll et al. 2009; Boquien et al. 2019), `SciPy` (Virtanen et al. 2020), `piecewise-regression` (Pilgrim 2021), `SAOImage ds9` (Joye & Mandel 2003), `Phyla/adjustText` (Flyamer et al. 2023).

## ORCID iDs

Ray Garner, III https://orcid.org/0000-0002-9426-7456
J. Christopher Mihos https://orcid.org/0000-0002-7089-8616
Paul Harding https://orcid.org/0000-0003-3442-6248

## References

Abdeen, S., Davis, B. L., Eufrasio, R., et al. 2022, MNRAS, 512, 366
Angthopo, J., Ferreras, I., & Silk, J. 2020, MNRAS, 495, 2720
Astropy Collaboration, Price-Whelan, A. M., Sipőcz, B. M., et al. 2018, AJ, 156, 123
Astropy Collaboration, Robitaille, T. P., Tollerud, E. J., et al. 2013, A&A, 558, A33
Athanassoula, E. 1992, MNRAS, 259, 328
Baba, J., Morokuma-Matsui, K., & Egusa, F. 2015, PASJ, 67, L4
Baba, J., Morokuma-Matsui, K., & Saitoh, T. R. 2017, MNRAS, 464, 246
Balogh, M. L., Morris, S. L., Yee, H. K. C., Carlberg, R. G., & Ellingson, E. 1999, ApJ, 527, 54
Beale, J. S., & Davies, R. D. 1969, Natur, 221, 531
Beauchamp, D., & Hardy, E. 1997, AJ, 113, 1666
Bell, E. F., & de Jong, R. S. 2000, MNRAS, 312, 497
Bertin, G., Lin, C. C., Lowe, S. A., & Thurstans, R. P. 1989, ApJ, 338, 78
Bianchi, L., Thilker, D. A., Burgarella, D., et al. 2005, ApJL, 619, L71
Boissier, S., Boselli, A., Buat, V., Donas, J., & Milliard, B. 2004, A&A, 424, 465
Bolzonella, M., Miralles, J.-M., & Pelló, R. 2000, A&A, 363, 476
Boquien, M., Burgarella, D., Roehlly, Y., et al. 2019, A&A, 622, A103
Bradley, L., Sipőcz, B., Robitaille, T., et al. 2023, astropy/photutils: 1.7.0, v1.7.0, Zenodo, doi:10.5281/zenodo.7804137
Brandt, T. D., & Draine, B. T. 2012, ApJ, 744, 129
Bruzual, A. G. 1983, ApJ, 273, 105
Bruzual, G., & Charlot, S. 2003, MNRAS, 344, 1000
Buta, R. J., Sheth, K., Athanassoula, E., et al. 2015, ApJS, 217, 32
Cedrés, B., Cepa, J., Bongiovanni, A., et al. 2013, A&A, 560, A59
Chabrier, G. 2003, PASP, 115, 763
Chandar, R., Chien, L.-H., Medit, S., et al. 2017, ApJ, 845, 78
Charlot, S., & Fall, S. M. 2000, ApJ, 539, 718
Contopoulos, G., & Papayannopoulos, T. 1980, A&A, 92, 33
Davis, B. L., Graham, A. W., & Seigar, M. S. 2017, MNRAS, 471, 2187
de Jong, R. S. 1996, A&A, 313, 377
Dixon, M. E. 1971, ApJ, 164, 411
Dobbs, C., & Baba, J. 2014, PASA, 31, e035
Dobbs, C. L., Adamo, A., Few, C. G., et al. 2017, MNRAS, 464, 3580
Dobbs, C. L., & Pringle, J. E. 2010, MNRAS, 409, 396
D'Onghia, E., Madau, P., Vera-Ciro, C., Quillen, A., & Hernquist, L. 2016, ApJ, 823, 4
D'Onghia, E., Vogelsberger, M., & Hernquist, L. 2013, ApJ, 766, 34
Egusa, F., Kohno, K., Sofue, Y., Nakanishi, H., & Komugi, S. 2009, ApJ, 697, 1870
Elmegreen, B. G., & Elmegreen, D. M. 1986, ApJ, 311, 554
Elmegreen, B. G., Elmegreen, D. M., & Montenegro, L. 1992, ApJS, 79, 37
Fisher, D., Franx, M., & Illingworth, G. 1995, ApJ, 448, 119
Fisher, D. B., & Drory, N. 2010, ApJ, 716, 942
Fisher, D. B., Drory, N., & Fabricius, M. H. 2009, ApJ, 697, 630
Flyamer, I., Xue, Z., Colin, et al. 2023, Phlya/adjustText: 0.8, v0.080, Zenodo, doi:10.5281/zenodo.7648985
Font, J., Beckman, J. E., Querejeta, M., et al. 2014, ApJS, 210, 2

Foyle, K., Rix, H.-W., Dobbs, C. L., Leroy, A. K., & Walter, F. 2011, ApJ, 735, 101
Foyle, K., Rix, H.-W., Walter, F., & Leroy, A. K. 2010, ApJ, 725, 534
Ganda, K., Peletier, R. F., McDermid, R. M., et al. 2007, MNRAS, 380, 506
Garner, R., Mihos, J. C., Harding, P., & Watkins, A. E. 2021, ApJ, 915, 57
Garner, R., Mihos, J. C., Harding, P., Watkins, A. E., & McGaugh, S. S. 2022, ApJ, 941, 182
González, R. A., & Graham, J. R. 1996, ApJ, 460, 651
González Delgado, R. M., Cerviño, M., Martins, L. P., Leitherer, C., & Hauschildt, P. H. 2005, MNRAS, 357, 945
González Delgado, R. M., Leitherer, C., & Heckman, T. M. 1999, ApJS, 125, 489
Grand, R. J. J., Kawata, D., & Cropper, M. 2012, MNRAS, 421, 1529
Haffner, L. M., Dettmar, R.-J., Beckman, J. E., et al. 2009, RvMP, 81, 969
Harris, C. R., Millman, K. J., van der Walt, S. J., et al. 2020, Natur, 585, 357
Herrera-Endoqui, M., Díaz-García, S., Laurikainen, E., & Salo, H. 2015, A&A, 582, A86
Hewitt, I. B., & Treuthardt, P. 2020, MNRAS, 493, 3854
Høg, E., Fabricius, C., Makarov, V. V., et al. 2000, A&A, 355, L27
Hunter, J. D. 2007, CSE, 9, 90
Joye, W. A., & Mandel, E. 2003, in ASP Conf. Ser. 295, Astronomical Data Analysis Software and Systems XII, ed. H. E. Payne, R. I. Jedrzejewski, & R. N. Hook (San Francisco, CA: ASP), 489
Knapen, J. H., & Beckman, J. E. 1996, MNRAS, 283, 251
Kormendy, J., Drory, N., Bender, R., & Cornell, M. E. 2010, ApJ, 723, 54
Kormendy, J., & Norman, C. A. 1979, ApJ, 233, 539
Lee, J. C., Whitmore, B. C., Thilker, D. A., et al. 2022, ApJS, 258, 10
Lin, C. C., & Shu, F. H. 1964, ApJ, 140, 646
Lin, L., Zou, H., Kong, X., et al. 2013, ApJ, 769, 127
Linden, S. T., & Mihos, J. C. 2022, ApJL, 933, L33
Lord, S. D., & Young, J. S. 1990, ApJ, 356, 135
MacArthur, L. A. 2005, ApJ, 623, 795
MacArthur, L. A., Courteau, S., Bell, E., & Holtzman, J. A. 2004, ApJS, 152, 175
Malin, D. F. 1977, AASPB, 16, 10
Martínez-García, E. E., & González-Lópezlira, R. A. 2011, ApJ, 734, 122
Martínez-García, E. E., & González-Lópezlira, R. A. 2015, HiA, 16, 323
Martínez-García, E. E., González-Lópezlira, R. A., & Bruzual-A, G. 2009, ApJ, 694, 512
Masset, F., & Tagger, M. 1997, A&A, 322, 442
Massey, P., Strobel, K., Barnes, J. V., & Anderson, E. 1988, ApJ, 328, 315
Matheson, T., Joyce, R. R., Allen, L. E., et al. 2012, ApJ, 754, 19
McKee, C. F., & Ostriker, E. C. 2007, ARA&A, 45, 565
Meidt, S. E., Rand, R. J., & Merrifield, M. R. 2009, ApJ, 702, 277
Meidt, S. E., Rand, R. J., Merrifield, M. R., Debattista, V. P., & Shen, J. 2008a, ApJ, 676, 899
Meidt, S. E., Rand, R. J., Merrifield, M. R., Shetty, R., & Vogel, S. N. 2008b, ApJ, 688, 224
Mihos, J. C., Durrell, P. R., Feldmeier, J. J., Harding, P., & Watkins, A. E. 2018, ApJ, 862, 99
Mihos, J. C., Harding, P., Spengler, C. E., Rudick, C. S., & Feldmeier, J. J. 2013, ApJ, 762, 82
Mihos, J. C., Keating, K. M., Holley-Bockelmann, K., Pisano, D. J., & Kassim, N. E. 2012, ApJ, 761, 186
Mo, H. J., Mao, S., & White, S. D. M. 1998, MNRAS, 295, 319
Mollá, M., Hardy, E., & Beauchamp, D. 1999, ApJ, 513, 695
Muggeo, V. M. R. 2003, Stat Med, 22, 3055
Noll, S., Burgarella, D., Giovannoli, E., et al. 2009, A&A, 507, 1793
Peletier, R. F., Falcón-Barroso, J., Bacon, R., et al. 2007, MNRAS, 379, 445
Peters, S. P. C., van der Kruit, P. C., Knapen, J. H., et al. 2017, MNRAS, 470, 427
Pettitt, A. R., Tasker, E. J., & Wadsley, J. W. 2016, MNRAS, 458, 3990
Pettitt, A. R., Tasker, E. J., Wadsley, J. W., Keller, B. W., & Benincasa, S. M. 2017, MNRAS, 468, 4189
Pilgrim, C. 2021, JOSS, 6, 3859
Querejeta, M., Schinnerer, E., Meidt, S., et al. 2021, A&A, 656, A133
Ragan, S. E., Moore, T. J. T., Eden, D. J., et al. 2018, MNRAS, 479, 2361
Rautiainen, P., & Salo, H. 1999, A&A, 348, 737
Renard, P., Siudek, M., Eriksen, M. B., et al. 2022, MNRAS, 515, 146
Rider, P. R. 1960, J. Amer. Statist. Assoc., 55, 148
Roberts, W. W. 1969, ApJ, 158, 123
Roberts, W. W., Roberts, M. S., & Shu, F. H. 1975, ApJ, 196, 381
Roškar, R., Debattista, V. P., Quinn, T. R., Stinson, G. S., & Wadsley, J. 2008a, ApJL, 684, L79
Roškar, R., Debattista, V. P., Stinson, G. S., et al. 2008b, ApJL, 675, L65
Ryder, S. D., Fenner, Y., & Gibson, B. K. 2005, MNRAS, 358, 1337
Salo, H., & Laurikainen, E. 2000, MNRAS, 319, 393
Sánchez-Blázquez, P., Rosales-Ortega, F., Diaz, A., & Sánchez, S. F. 2014a, MNRAS, 437, 1534
Sánchez-Blázquez, P., Rosales-Ortega, F. F., Méndez-Abreu, J., et al. 2014b, A&A, 570, A6
Sánchez-Gil, M. C., Jones, D. H., Pérez, E., et al. 2011, MNRAS, 415, 753
Scarano, S., & Lépine, J. R. D. 2013, MNRAS, 428, 625
Seigar, M. S., & James, P. A. 1998, MNRAS, 299, 685
Sellwood, J. A. 2011, MNRAS, 410, 1637
Sellwood, J. A., & Binney, J. 2002, MNRAS, 336, 785
Sellwood, J. A., & Carlberg, R. G. 1984, ApJ, 282, 61
Sellwood, J. A., & Carlberg, R. G. 2019, MNRAS, 489, 116
Sellwood, J. A., & Kahn, F. D. 1991, MNRAS, 250, 278
Sellwood, J. A., & Masters, K. L. 2022, ARA&A, 60, 36
Sellwood, J. A., & Sparke, L. S. 1988, MNRAS, 231, 25
Sheth, K., Regan, M., Hinz, J. L., et al. 2010, PASP, 122, 1397
Shu, F. H. 2016, ARA&;A, 54, 667
Shu, F. H., Milione, V., Gebel, W., et al. 1972, ApJ, 173, 557
Skrutskie, M. F., Cutri, R. M., Stiening, R., et al. 2006, AJ, 131, 1163
Slater, C. T., Harding, P., & Mihos, J. C. 2009, PASP, 121, 1267
Stothert, L., Norberg, P., Baugh, C. M., et al. 2018, MNRAS, 481, 4221
Sygnet, J. F., Tagger, M., Athanassoula, E., & Pellat, R. 1988, MNRAS, 232, 733
Thilker, D. A., Bianchi, L., Meurer, G. R., et al. 2007, ApJS, 173, 538
Toomre, A. 1964, ApJ, 139, 1217
Vale Asari, N., Couto, G. S., Cid Fernandes, R., et al. 2019, MNRAS, 489, 4721
Virtanen, P., Gommers, R., Oliphant, T. E., et al. 2020, NatMe, 17, 261
Vogel, S. N., Kulkarni, S. R., & Scoville, N. Z. 1988, Natur, 334, 402
Wada, K., Baba, J., & Saitoh, T. R. 2011, ApJ, 735, 1
Waller, W. H., Bohlin, R. C., Cornett, R. H., et al. 1997, ApJ, 481, 169
Watkins, A. E., Mihos, J. C., & Harding, P. 2016, ApJ, 826, 59
Watkins, A. E., Mihos, J. C., & Harding, P. 2017, ApJ, 851, 51
White, S. D. M., & Frenk, C. S. 1991, ApJ, 379, 52
Williams, D. 2001, Weighing the Odds: A Course in Probability and Statistics, 165 (Cambridge: Cambridge Univ. Press)
Wood, S. N. 2001, Biometrics, 57, 240
Worthey, G. 1994, ApJS, 95, 107
Xu, J.-L., Zhang, C.-P., Yu, N., et al. 2021, ApJ, 922, 53